Supplementary Materials for

Recruited macrophages elicit atrial fibrillation

Maarten Hulsmans *et al.*

Corresponding authors: Maarten Hulsmans, mhulsmans@mgh.harvard.edu; Kamila Naxerova, naxerova.kamila@mgh.harvard.edu; Matthias Nahrendorf, mnahrendorf@mgh.harvard.edu

This PDF file includes:

Other Supplementary Material for this manuscript includes the following:

Data S1 to S9

Materials and Methods

Human samples for scRNA-seq

Human left atrial appendages were obtained from well-characterized patients undergoing cardiac surgery at the Massachusetts General Hospital. The enrollment specifically involved patients with or without persistent AFib. Patients with AFib had pre-existing moderate to severe mitral valve regurgitation (MR). Control patients never had AFib. General inclusion criterion was age >18 years, with no specific exclusion criteria on the basis of sex, gender, race or ethnicity. Human tissue collection was conducted according to the Declaration of Helsinki and was approved by the Mass General Brigham Institutional Review Board (2019P002446). All patients gave written, informed consent before sample collection, as required. The excised atrial tissue samples were placed in a specimen container containing ice-cold PBS in the operating room and processed immediately for single-cell transcriptional profiling.

Human samples for histology

Existing formalin-fixed paraffin-embedded (FFPE) blocks of human left atrial samples, collected during cardiac surgery or autopsy at different clinical sites (Massachusetts General Hospital, Brigham and Women's Hospital, University Hospital Wuerzburg, University Hospital Goettingen and John Radcliffe Hospital), were obtained for histology with approval from the local Research Ethics Committee at Mass General Brigham (2012P001135 and 2019P003227), University Hospital Wuerzburg (59/26-sc), University Hospital Goettingen (14/9/11), and John Radcliffe Hospital (07/Q1607/38 and 18/SW/0243). Patients were categorized into four groups based on their MR and/or AFib diagnoses. MR was defined significant if it was recorded as moderate or severe by echocardiography prior to sampling. Recorded electrocardiographic data of paroxysmal, persistent or permanent Afib prior to sampling was defined as Afib. Left and right atria were defined as dilated if diameter, area, or volume were larger than reported upper reference values (*51*, *52*). Detailed patient characteristics of the scRNA-seq and histology cohorts are shown in tables S1 and S3, respectively.

Mice

Wildtype C57BL/6 (stock 000664), B6.129P2(Cg)-*Cx3cr1*$^{tm2.1(cre/ERT2)Litt}$/WganJ (*Cx3cr1*^{CreER}, stock 021160), B6.Cg-*Gt(ROSA)26Sor*$^{tm9(CAG-tdTomato)Hze}$/J (*Ai9*$^{fl/fl}$, stock 007909), B6.129S4-*Ccr2*^{tm1Ifc}/J (*Ccr2*$^{-/-}$, stock 004999), B6.SJL-*Ptprc*^{a} *Pepc*^{b}/BoyJ (*Cd45.1*, stock 002014) and B6.129S6(Cg)-*Spp1*^{tm1Blh}/J (*Spp1*$^{-/-}$, stock 004936) were purchased from the Jackson Laboratory. Genotyping for each strain was performed as described on the Jackson Laboratory website. All experiments were performed with 8-to-12-week-old male and female animals and using age- and sex-matched groups. Where appropriate, mice were randomly assigned to interventions. All mice were group-housed under standard conditions with free access to food and water. All animal experiments were approved by the Institutional Animal Care and Use Committee at the Massachusetts General Hospital (2014N000078).

In vivo interventions

<u>HOMER mouse model</u>

To induce atrial remodeling and a disease condition that combines all three clinical risk factors (hypertension, obesity, and mitral valve regurgitation (HOMER)), mice first underwent surgery to generate MR, were then fed a high-fat diet, and finally had hypertension induced. In detail,

mice were anesthetized (2.5% isoflurane in 95% O_2), intubated, ventilated, and placed on a heating pad. A left lateral thoracotomy at the level of the second or third intercostal space was performed and the pericardial sack was opened to gain access to the heart. The mouse was then rotated to the right in order to expose the anterior and lateral aspects of the left atrium and ventricle. The left atrium was carefully elevated and an 8.0 suture was inserted into the inferior part of the left atrium just above the mitral annulus. The needle was guided through the mitral valve without visual control and exerted through the left ventricle just inferior of the mitral annulus and superior to the left circumflex artery. A 5-throw surgical knot was performed, thereby mechanically snaring the mitral valve to the left ventricular wall. The intercostal space and skin were surgically closed with a 5.0 suture. The animals were allowed to recover with oxygen on a heating pad until extubation. For sham surgery, mice underwent left thoracotomy as described above, and the pericardium was incised. In an additional cohort of sham-operated mice, the same surgical steps were performed as described above (including needle insertion through the left atrium and mitral valve as well as exertion through the left ventricle) but without tying a surgical knot. Four weeks after surgery, either regular chow diet or high-fat diet (Research Diets, D12492) was initiated and continued for 17 weeks. Finally, 20 weeks after mitral valve surgery, animals were exposed to continuous infusion of either saline or angiotensin 2 (Sigma-Aldrich, 1 µg/kg/min) for 1 week via a subcutaneously implanted osmotic minipump (Alzet).

EP study

EP studies were performed under general anesthesia with isoflurane. A Millar EPR-800 octapolar catheter was inserted into the right jugular vein and positioned in the right atrium and ventricle. Sinus node function was determined by measuring the sinus node recovery time following 30 s of pacing at two cycle lengths (100 and 80 ms). The Wenckebach cycle length was measured with progressively faster atrial pacing rates. Atrial and atrioventricular node effective refractory periods were measured using programmed electrical stimulation with overdrive pacing trains at 100 ms followed by single extrastimuli. Provocative testing for arrhythmia induction was performed with double extrastimuli (S1-S2-S3) as well as burst pacing at gradually faster rates to a pacing cycle length of 10 ms. Two different drive-train cycle lengths (S1) were used (120 ms and 100 ms), and each set of double extrastimuli was performed twice. Burst pacing was performed twice at a duration of 3 s and then 6 s, with cycle length starting at 50 ms and progressing to 10 ms in intervals of 5 ms. AFib was defined as a rapid atrial rhythm with an atrial rate faster than the ventricular rate and irregular ventricular response (R-R intervals). The duration was measured from the end of the pacing cycle to the first P wave. A mouse was deemed inducible if it had at least one episode of AFib lasting more than 500 ms. The total AFib burden for any given mouse was obtained by summing all episodes of AFib >250 ms over the course of the entire EP study.

Ambulatory ECG telemetry

Continuous ambulatory ECG telemetry was performed by implanting an ETA-F10 transmitter (Data Sciences International) during general anesthesia with isoflurane. The transmitter was implanted in the abdomen and the leads were tunneled subcutaneously to the upper right and lower left chest resulting in a lead II position. Telemetry data were recorded continuously via a receiver placed under the mouse cage. Data were analyzed using LabChart Pro v8 (AD Instruments) software.

Blood pressure measurements

Blood pressure in conscious mice was measured with a non-invasive tail-cuff system (Kent Scientific Corporation) per manufacturer's instructions.

Bone marrow transplantation

For whole bone marrow transplants, recipient mice were lethally irradiated (single dose of 10 Gy) and received 4×10^6 bone marrow cells from donor mice by intravenous injection. Mice were exposed to the HOMER protocol 8 weeks after transplantation.

Tamoxifen injection

Tamoxifen (Sigma-Aldrich) was administered as a solution in corn oil (Sigma-Aldrich) to *Cx3cr1*$^{CreER/+}$*Ai9*$^{fl/+}$ mice by intraperitoneal injection. Animals received five doses (100 µl each) of 2 mg tamoxifen with 24 hours between doses.

Synthesis of CCL2-Fc

A plasmid was generated to encode murine CCL2 mutant P8A (*35*) fused to the N terminus of a mouse CH2-CH3 IgG2c Fc domain bearing three point mutations (LALAPG) that ablate Fc/FcR-mediated effector functions. This plasmid was transfected into Expi293 cells to produce CCL2-Fc, a protein capable of inhibiting endogenous CCL2 from binding CCR2. The construct was then isolated by protein A sepharose affinity chromatography and dialyzed into PBS solution to a concentration of 1 mg/ml. SDS-PAGE confirmed that this construct was produced as a monomeric protein and in vitro assays confirmed specific binding to CCR2.

Cells

Cell collection

Mouse peripheral blood was collected by retro-orbital bleeding using heparinized capillary tubes, and red blood cells were lysed with 1X red blood cell lysis buffer (BioLegend). For organ harvest, mice were perfused through the left ventricle with 10 ml of ice-cold PBS. Hearts were then excised and left atrial tissues were microdissected using a dissection microscope. After harvest, tissues were minced into small pieces and subjected to enzymatic digestion with 450 U/ml of collagenase I, 125 U/ml of collagenase XI, 60 U/ml of DNase I, and 60 U/ml of hyaluronidase (all Sigma-Aldrich) for 40 min at 37°C under agitation. Tissues were triturated and cells were filtered through a 40-µm nylon mesh, washed, and centrifuged (340*g* for 7 min) to obtain single-cell suspensions.

Flow cytometry

To detect leukocyte subsets in processed blood samples, cell suspensions were stained at 4°C in FACS buffer (PBS supplemented with 0.5% bovine serum albumin) with anti-CD11b, -CD19, -CD90.2, -CD115, -Ly6C, and -Ly6G. For non-cardiomyocyte cell staining on processed heart samples, isolated cells were stained with anti-CCR2, -CD9, -CD11b, -CD31, -CD45, -CD64, -CD146, -MEFSK4, -MHCII, and/or -TREM2. Detailed antibody information is provided in table S10. DAPI was used as a cell viability marker. Data were acquired on an LSRII (BD Biosciences) and analyzed with FlowJo software.

Flow cytometry gating

Blood monocytes were identified as $CD19^{-}CD90.2^{-}CD11b^{+}CD115^{hi}Ly6C^{lo/hi}$, neutrophils as $CD19^{-}CD90.2^{-}CD11b^{+}CD115^{lo/int}Ly6G^{+}$, and B and T cells as $CD19^{+}CD90.2^{-}$ and $CD19^{-}CD90.2^{+}$, respectively. Cardiac endothelial cells were identified as $CD31^{+}CD45^{-}$, fibroblasts as $CD31^{-}CD45^{-}CD146^{-}MEFSK4^{+}$, mural cells as $CD31^{-}CD45^{-}MEFSK4^{lo/int}CD146^{+}$, neutrophils as $CD45^{+}CD11b^{+}CD64^{-}CCR2^{-}$, and monocytes as $CD45^{+}CD11b^{+}CD64^{-}CCR2^{+}$. Cardiac macrophages were identified as $CD45^{+}CD11b^{+}CD64^{+}$ and were further parsed by CCR2, MHCII, CD9, TREM2, YFP, and Td.

Cell sorting

Cardiac cell suspensions were stained to identify the indicated cell populations and cells were sorted on a FACSAria II cell sorter (BD Biosciences) directly into RLT Plus lysis buffer (Qiagen).

Human and mouse scRNA-seq

Tissue preparation

For human scRNA-seq, cardiac tissues were minced into small pieces and subjected to enzymatic digestion with 450 U/ml of collagenase I, 60 U/ml of DNase I, and 60 U/ml of hyaluronidase (all Sigma-Aldrich) for 1 hour at 37°C under mild agitation. Digested tissues were triturated, filtered, washed, and centrifuged (340*g* for 7 min) to obtain single-cell suspensions. Red blood cells were lysed with ACK buffer (Lonza). For mouse scRNA-seq, cardiac tissues were processed as described above. Two male mice were pooled for each sequencing replicate. Cell suspensions were then stained with three viability dyes (DAPI, calcein, and VDR, all ThermoFisher Scientific) as previously described (*53*, *54*). Viable ($DAPI^{-}$), metabolically active ($calcein^{+}$), nucleated (VDR^{+}) single cells were FACS-purified from digested tissues on a FACSAria II cell sorter and subsequently loaded on a 10X Genomics Chromium Single Cell B or G chip as outlined by the 10X Genomics Chromium Single Cell 3′ Reagent kits v3 or v3.1 user guide. Libraries were prepared according to the manufacturer's protocol with appropriate modifications to PCR cycles based on the calculated cDNA concentration. Constructed libraries were validated and quantified with the Agilent High Sensitivity DNA chip and by real-time qPCR and subsequently sequenced on an Illumina NextSeq 500 in high-output mode or an Illumina NovaSeq 6000 system as recommended by 10X Genomics.

Pre-processing scRNA-seq data

The sequencing reads for the human samples were aligned to the GRCh38 reference genome and processed with 10X Genomics Cell Ranger 6.0.2, which generated a gene-cell barcode count matrix for each sample. With the output from Cell Ranger, Seurat 4.0 (*55*, *56*) was used for further analysis. Quality-control metrics were first applied to filter out low-quality cells and rarely expressed genes. Specifically, this process removed cells that expressed fewer than 250 genes or had fewer than 500 unique molecular identifiers (UMIs), as well as those with greater than 25% of total UMI count from mitochondrial genes. Genes expressed in fewer than 10 cells were also filtered out. Count normalization was performed with the R package sctransform (*57*), followed by an integration workflow (*55*) which aimed to identify shared cell states present across all samples under consideration. Principal component analysis was carried out on the integrated data, and the top 40 principal components were used to cluster the cells. The FindMarkers function in Seurat was used to identify markers for each cluster and the

FindConservedMarkers function was used to identify markers conserved across the groups within each cluster. In both functions, a logistic regression model coupled with a likelihood ratio test was used to determine the differentially expressed genes in a given cluster compared to all other cells. The scRNA-seq data for the mouse samples were analyzed in the same way as detailed above except that the reference genome and versions of Cell Ranger and Seurat used were GRCm38 (mm10), Cell Ranger 3.0.2 or 7.0.1 and Seurat 3.1 or 4.1, respectively, and that slightly different filtering thresholds were applied. In particular, cells expressing fewer than 200 genes (as well as those with greater than 25% of total UMI count from mitochondrial genes) and genes expressed in fewer than three cells were filtered out.

Differential expression and gene set enrichment analyses

To detect differentially expressed genes between groups of cells with different disease conditions, pseudobulk differential expression analyses (*58*) were performed, taking into account biological replicates in our data sets. Specifically, for a given cell cluster, the cells and the UMI counts were aggregated to the sample level and the differential expression analysis was carried out with a quasi-likelihood *F* test based on the generalized linear model implementation of edgeR 3.34.1 (*10*, *59*, *60*). The output of the differential expression analysis was used to rank the genes by their fold change values. This rank list became the input for the gene set enrichment analysis (GSEA), which was performed with the GSEAPreranked tool from GSEA 4.2.0 (*11*, *61*) and the collections of gene sets in the molecular signatures database MSigDB 7.4 or 7.5 (*11*, *62*).

Weighted correlation network analysis and overrepresentation analysis

The R package WGCNA 1.70-3 (*12*, *63*) was used to identify groups of genes (gene modules) with highly correlated expressions and significant up- or downregulation in the diseased condition. Overrepresentation analysis (*64*) from the R package clusterProfiler 4.1.4 (*65*) was used to identify the gene sets that were overrepresented in these gene modules. GSEA as implemented in the R package clusterProfiler 4.1.4 (*65*) was used in Fig.1D and fig. S3C.

Interactions between cells from different lineages

CellPhoneDB 2.1.4 (*36*, *66*) was used to infer interlineage cell–cell interactions.

Imaging and histology

Cardiac MRI

MRI was performed with a 4.7-Tesla horizontal bore Pharmascan system (Bruker) equipped with a custom-built mouse cardiac coil (Rapid Biomedical) to obtain cine images of the left atrial and ventricular short axes. ECG and respiratory gating (SA Instruments), a gradient echo FLASH-sequence and a dedicated mouse cardiac volume coil in bird cage design were used. Imaging parameters were as follows: echo time (TE), 2.7 to 5 ms; 16 frames per RR interval (TR 7.0-15 ms depending on heart rate); in-plane resolution, 150×150 µm; slice thickness, 1 mm; NEX 4; flip angle, 30 degrees. Anatomical and functional parameters were quantified using Horos software.

Cardiac ultrasound

Doppler ultrasound was used to assess successfully induced MR. Mice were imaged under general anesthesia using a GE Healthcare Vivid E90 system equipped with a 15 MHz linear

probe (L8-18i-D) and the mitral Doppler inflow spectrum was recorded from the parasternal long axis view.

Mouse histology

To detect atrial fibrosis, hearts were embedded in OCT compound and frozen 7-µm sections were stained with Masson's trichrome. Briefly, sections were fixed with 10% formalin for 30 min at room temperature and incubated in Bouin's fixative solution (Electron Microscopy Sciences) overnight at room temperature, and the nuclei were stained with a mixture of Weigert's iron hematoxylin solution A and B (Electron Microscopy Sciences). The sections were then stained with Biebrich scarlet-acid fuchsin (StatLab), followed by phosphomolybdic acid/phosphotungstic acid solution (Sigma-Aldrich) and aniline blue stain (StatLab). TUNEL staining was carried out by using an In Situ Cell Death Detection kit (Roche) according to the manufacturer's protocol. For immunofluorescent staining, sections were stained with rabbit anti-mouse collagen I, rat anti-mouse CD68, rabbit anti-mouse Ki67, and/or FITC anti-mouse αSMA overnight at 4°C, followed by a biotinylated goat anti-rabbit IgG antibody and streptavidin DyLight 594, and/or an Alexa Fluor 488 goat anti-rat IgG antibody for 1 hour at room temperature. Detailed antibody information is provided in table S11. The nuclei were stained with DAPI. All slides were scanned by a digital slide scanner NanoZoomer 2.0RS (Hamamatsu). To analyze cellular signals in mice, six fields of views (FOV) from the left atrium per animal were exported at 40X using NanoZoomer NDP.view2 software. For each FOV, the percentage of positive signal was measured using ImageJ v2.9.0 (NIH) software. $Ki67^+$ and $TUNEL^+$ cells were manually counted per FOV.

Human histology

Left atrial FFPE samples were obtained from five different clinical sites (Massachusetts General Hospital, Brigham and Women's Hospital, University Hospital Wuerzburg, University Hospital Goettingen and John Radcliffe Hospital) and sectioned at 5 µm. The sections were then deparaffinized and rehydrated before immunofluorescent staining. Heat-induced antigen retrieval was performed using Retrievagen A (pH6.0, BD Biosciences) and the sections were permeabilized with 0.3% Triton X-100 in PBS for 10 min at room temperature. After the sections were blocked with 2% normal horse serum and 2% normal goat serum in PBS, primary antibodies, mouse anti-human CCR2, and rabbit anti-human CD68 were incubated at 4°C overnight. For SPP1/COL1A1 detection, left atrial FFPE sections were treated with citrate unmasking solution (Cell Signaling) followed by staining with primary antibodies mouse anti-human SPP1 and rabbit anti-human COL1A1 at 4°C overnight. The sections were then stained with a biotinylated horse anti-mouse IgG antibody and streptavidin DyLight 594, and an Alexa Fluor 488 goat anti-rabbit IgG antibody. Detailed antibody information is provided in table S11. The nuclei were stained with DAPI. To remove lipofuscin and autofluorescence signal, tissues were incubated with TrueBlack Plus quencher (Biotium) for 10 min at room temperature. All the slides were scanned using the NanoZoomer 2.0RS scanner or imaged using a Zeiss LSM 800 Airyscan confocal microscope.

$CCR2^+$ macrophage density analysis

Atrial macrophages were enumerated in 3-5 FOVs per patient from 149 clinical cases using semiautomated image analysis (*67*). During a preprocessing stage, we reduced fluorescence background and increased the signal contrast to optimize cell segmentation. Image contrast was

optimized using a contrast-limited adaptive histogram equalization algorithm and the images were spatially filtered and denoised. A watershed algorithm was used to count individual cells and a size threshold was employed to reject areas smaller than cells. After segmentation of macrophages in the Alexa Fluor 488 channel encoding for CD68, the resulting areas were considered in the DyLight 594 channel encoding for CCR2 to generate a reduced segmentation mask. The CCR2 signal within individual CD68 masks was then calculated and macrophages were marked positive for CCR2 if the value was above a threshold determined using the standard deviation of the CCR2 signal across the entire image. Segmentation results were inspected individually for quality control. Software (*67*) was written in Python 3.7.4 using OpenCV, NumPy and Scikit-learn packages.

Human RNA in situ hybridization

In situ hybridization was performed on a Leica Biosystems BOND RX system using human FFPE samples and the RNAscope 2.5 LS Duplex assay with RNAscope 2.5 LS Green Accessory pack (both Advanced Cell Diagnostics) following the manufacturer's protocol with minor modifications. These modifications include an antigen retrieval step for 15 min at 88°C and a protease incubation step for 15 min at 40°C. Each FFPE sample was first stained with the RNAscope 2.5 LS Duplex positive (Hs-PPIB-C1, Hs-POLR2A-C2) and negative (DapB-C1, DapB-C2) control probes to assess tissue quality. If the sample passed quality control metrics (i.e., sufficient positive control probe signal in the absence of negative control probe signal), the adjacent tissue section was stained with the RNAscope 2.5 LS Hs-CD68-C1 (Cat# 560598) and Hs-SPP1-C2 (Cat# 420108-C2) probes to detect *CD68* and *SPP1* signal, respectively. For quantification, three FOVs per sample were exported at 40X using NanoZoomer NDP.view2 software. For each FOV, $SPP1^{+}CD68^{+}$ macrophages were manually counted using ImageJ software. Cells with more than two spots for a given marker were considered positive for that marker.

Molecular biology

Real-time qPCR

Total RNA from left atrial tissue was extracted using the RNeasy Plus Mini kit or from FACS-purified cells using the RNeasy Plus Micro kit (both Qiagen) according to the manufacturer's protocol. First-strand cDNA was synthesized using the High-Capacity RNA-to-cDNA kit (ThermoFisher Scientific) according to the manufacturer's instructions. TaqMan Fast Universal PCR Master Mix and TaqMan gene expression assays (both ThermoFisher Scientific) were used to quantify target genes. The relative changes were normalized to *Gapdh* mRNA using the $2^{-\Delta\Delta Ct}$ method.

Statistics and reproducibility

Results are shown as means ± SEM. Statistical analysis was performed using GraphPad Prism 9.5.1. Where appropriate, statistical outliers identified by the ROUT method (Q=1%) were excluded. Statistical tests included two-tailed Student's *t* tests, two-tailed paired *t* tests, ANOVA followed by Dunnett's or Tukey's multiple comparisons test, two-tailed Mann–Whitney tests, two-tailed Wilcoxon matched-pairs signed rank tests, and Kruskal–Wallis tests followed by Dunn's multiple comparisons test (the latter three if Gaussian distribution was not assumed). For correlation analysis, the r or ρ values were computed using two-tailed Pearson correlation coefficients or two-tailed Spearman correlation coefficients, respectively. P-values of 0.05 or

less were considered to denote significance. Animal group sizes were as low as possible and empirically chosen. No statistical methods were used to predetermine sample size. Animals were randomly assigned to treatment groups and analyzed in a blinded fashion where appropriate.

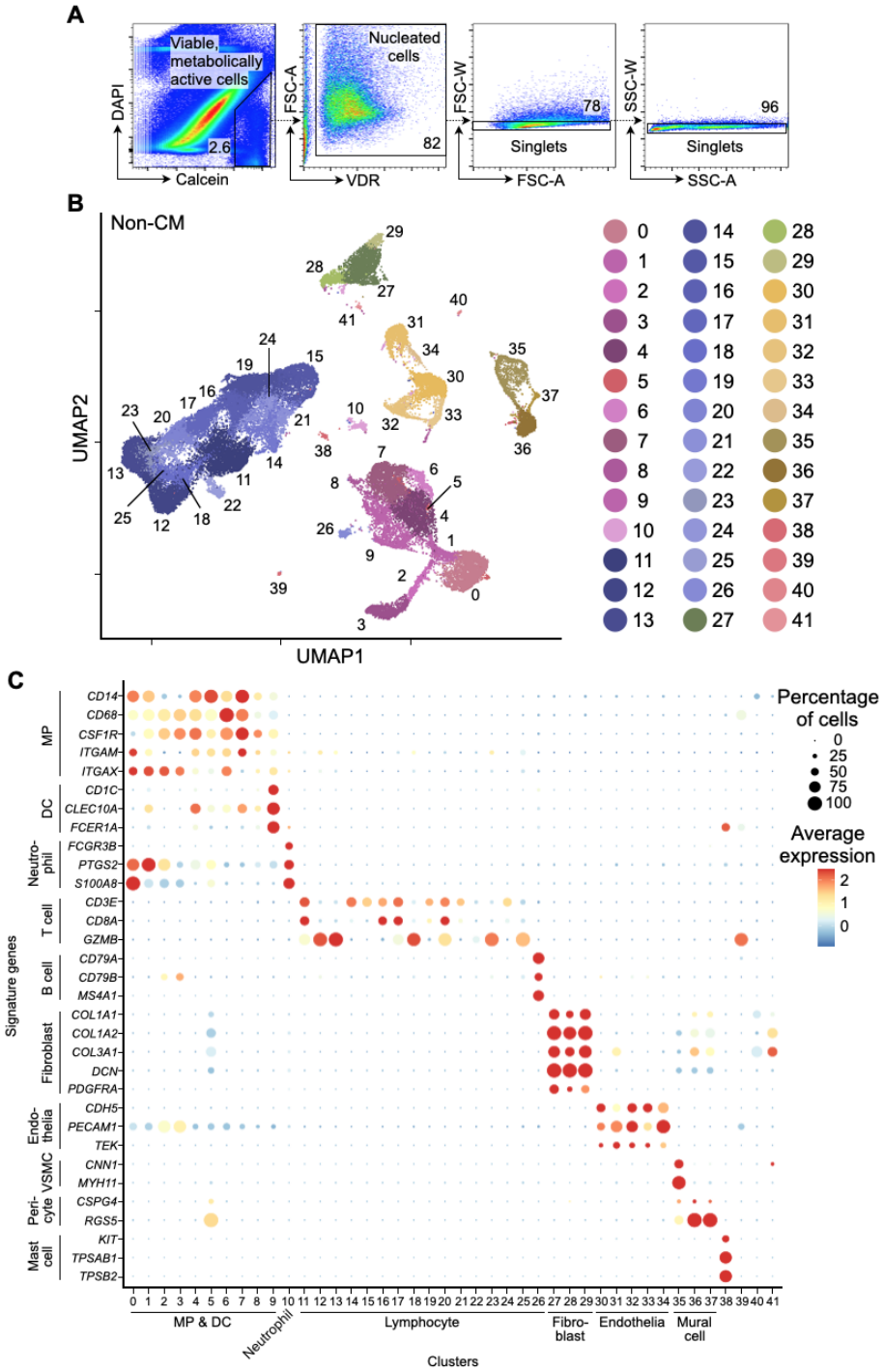

Fig. S1. Isolating and annotating human left atrial non-cardiomyocytes. (**A**) Representative plots of the flow cytometry gating strategy for isolating single, viable non-cardiomyocytes (non-CM) from human left atrial appendages. VDR, vybrant dyecycle ruby. (**B**) Clustering of 41,609 non-CM from five controls and seven AFib left atrial appendages. (**C**) Dot plot annotating non-CM clusters by signature gene expression. Color denotes *z*-score of average gene expression (red: high; blue: low) and circle size indicates percentage of cells expressing the gene. Mural cells collectively refer to smooth muscle cells and pericytes of the vasculature.

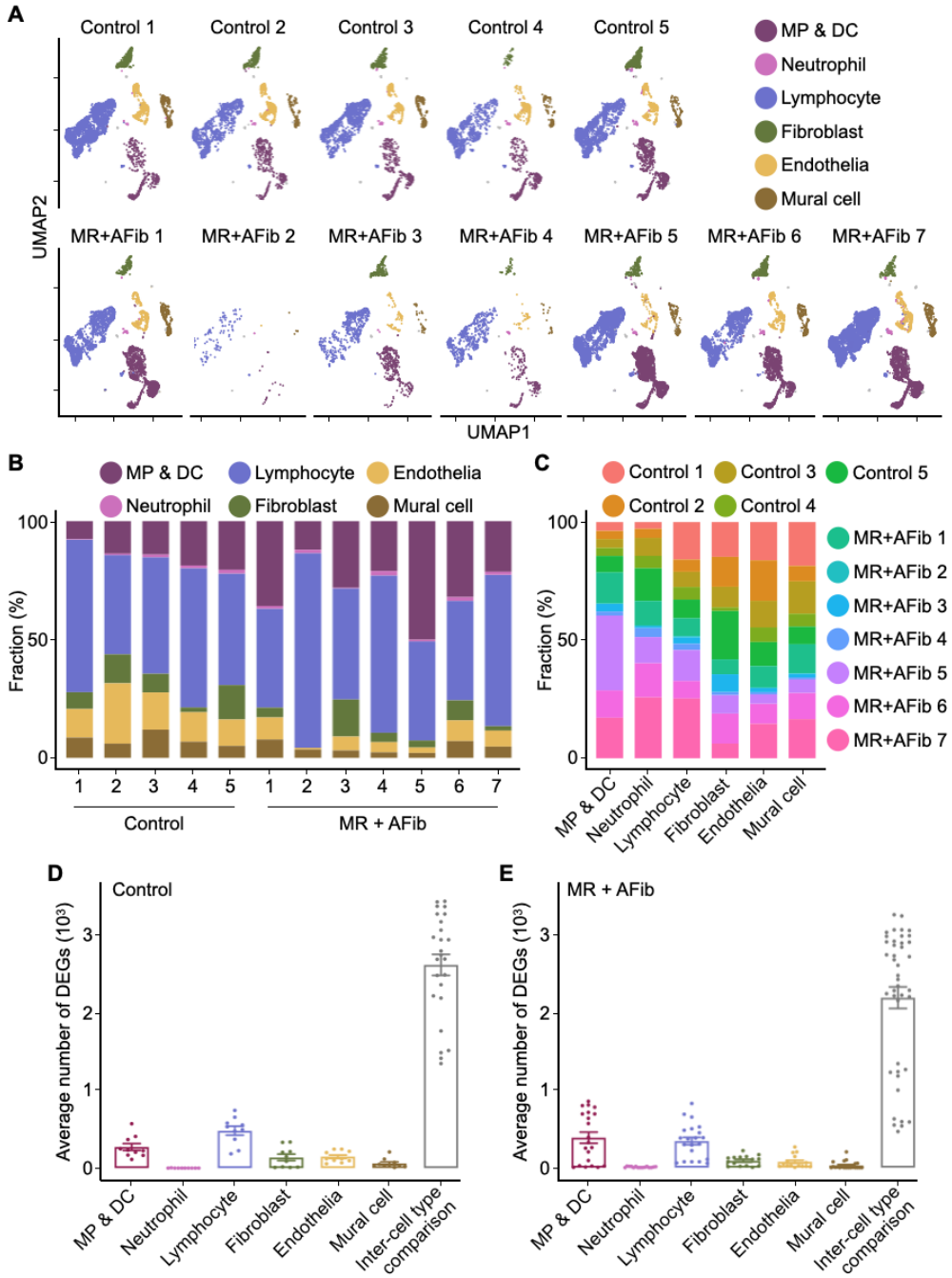

Fig. S2. Detailed description of human scRNA-seq data. (**A**) UMAP plots of individual patients delineating six major cardiac cell types. (**B**) Fraction of cells belonging to the different cell types for each individual patient. (**C**) Proportion of cells originating from each patient for all six cardiac cell types. (**D**) Average number of differentially expressed genes (DEGs, adjusted *P*-value < 0.01 based on Bonferroni correction) for all six cell types by pairwise comparison of the different control samples. The bar on the right indicates the average number of DEGs by pairwise comparison of the fibroblast and MP/DC cluster for all control samples. Each dot represents the number of DEGs between a pair of samples. The differential gene expression analysis was performed with Seurat's FindMarkers function. (**E**) Same analysis as in (D) but for AFib patients. All bar graph data are means ± SEM with individual values for data distribution.

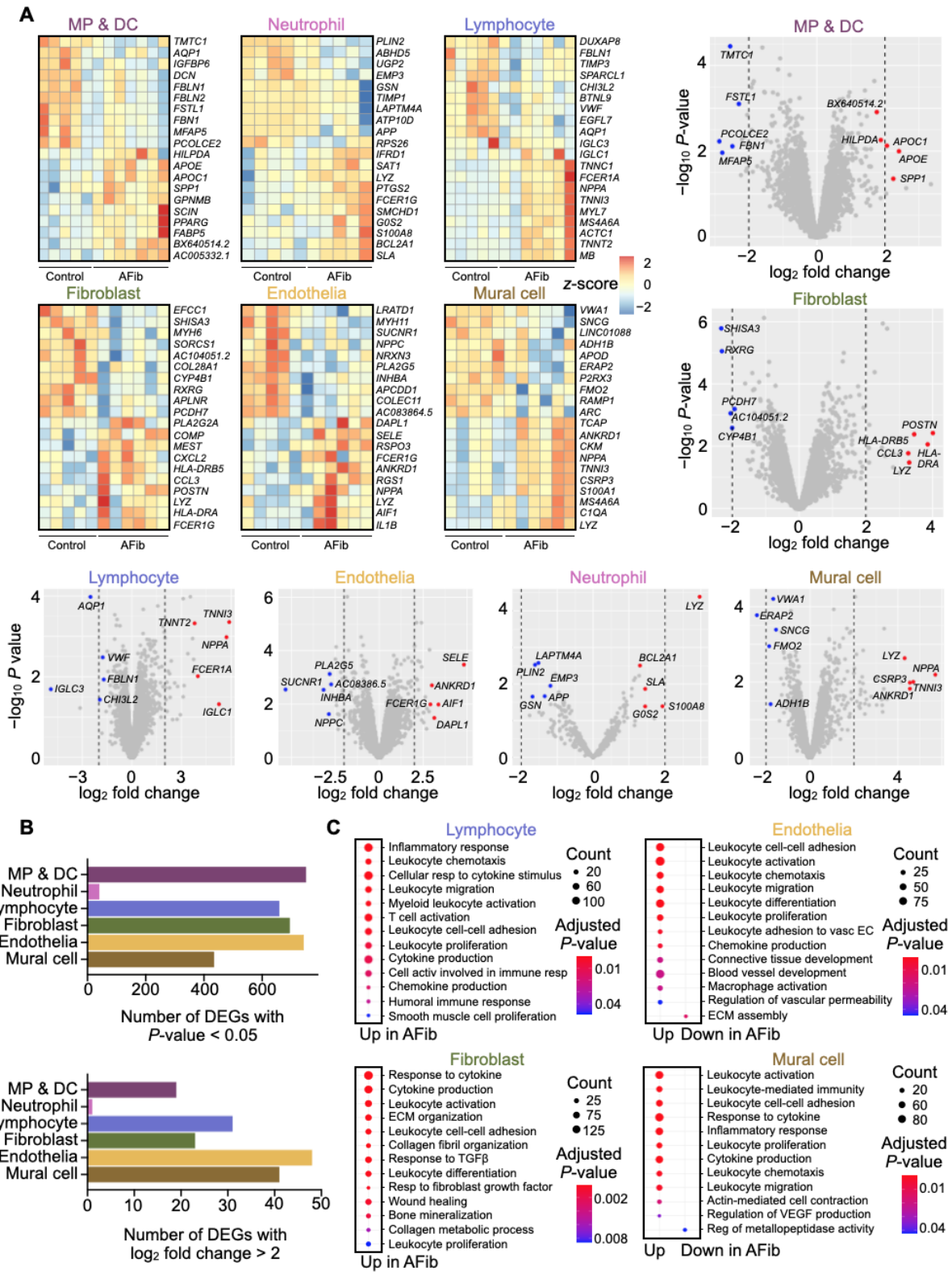

Fig. S3. Transcriptional changes in non-cardiomyocyte clusters in human AFib.
(**A**) Heatmaps of the 10 most upregulated and the 10 most downregulated genes in each cell type, comparing AFib patients with controls. Only genes with unadjusted *P*-values < 0.05 were included. Each column represents a patient. Color denotes *z*-scores of the log-transformed

normalized counts for each individual patient. Panel further shows all genes in volcano plots for the same cells in all patients, highlighting the top five upregulated (downregulated) genes in AFib with the highest $\log_2$-fold change and *P*-value < 0.05 in red (blue). (**B**) Number of DEGs in AFib patients versus control cases, showing genes with unadjusted *P*-values < 0.05 (upper panel) and genes with a $\log_2$-fold change > 2 (lower panel) for each respective cell population. (**C**) Significant gene ontology biological process (GOBP) gene sets up- or downregulated in AFib patients from GSEA of lymphocyte, fibroblast, endothelial, and mural cell clusters (a similar analysis for MP/DCs is shown in Fig. 1D). Circle size denotes number of genes in the core enrichment set that belong to a given GOBP gene set.

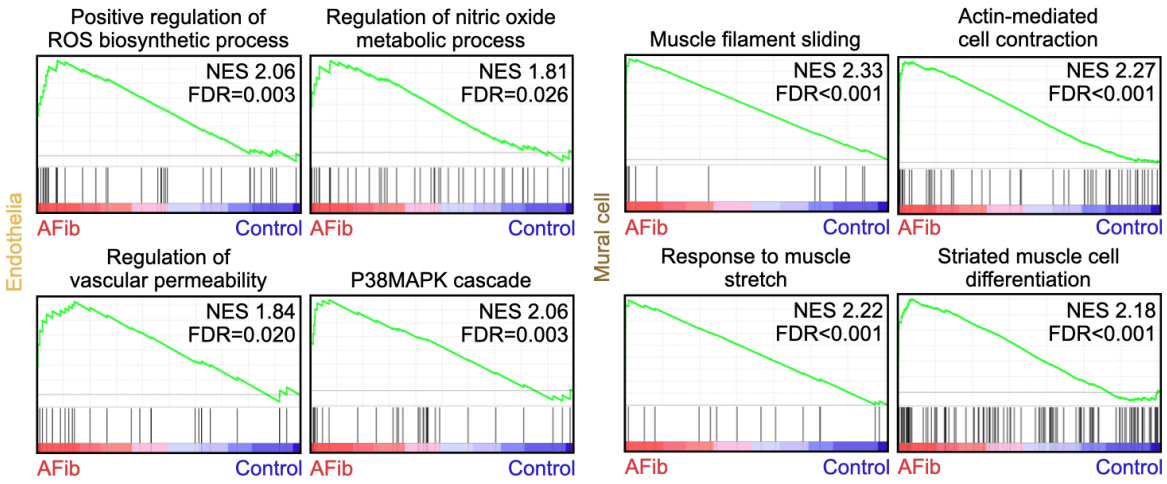

Fig. S4. Ischemia and vascular remodeling in diseased left atrial tissue. GSEA results of endothelia (left) and mural cells (right) in five controls versus seven AFib patients. NES, normalized enrichment score.

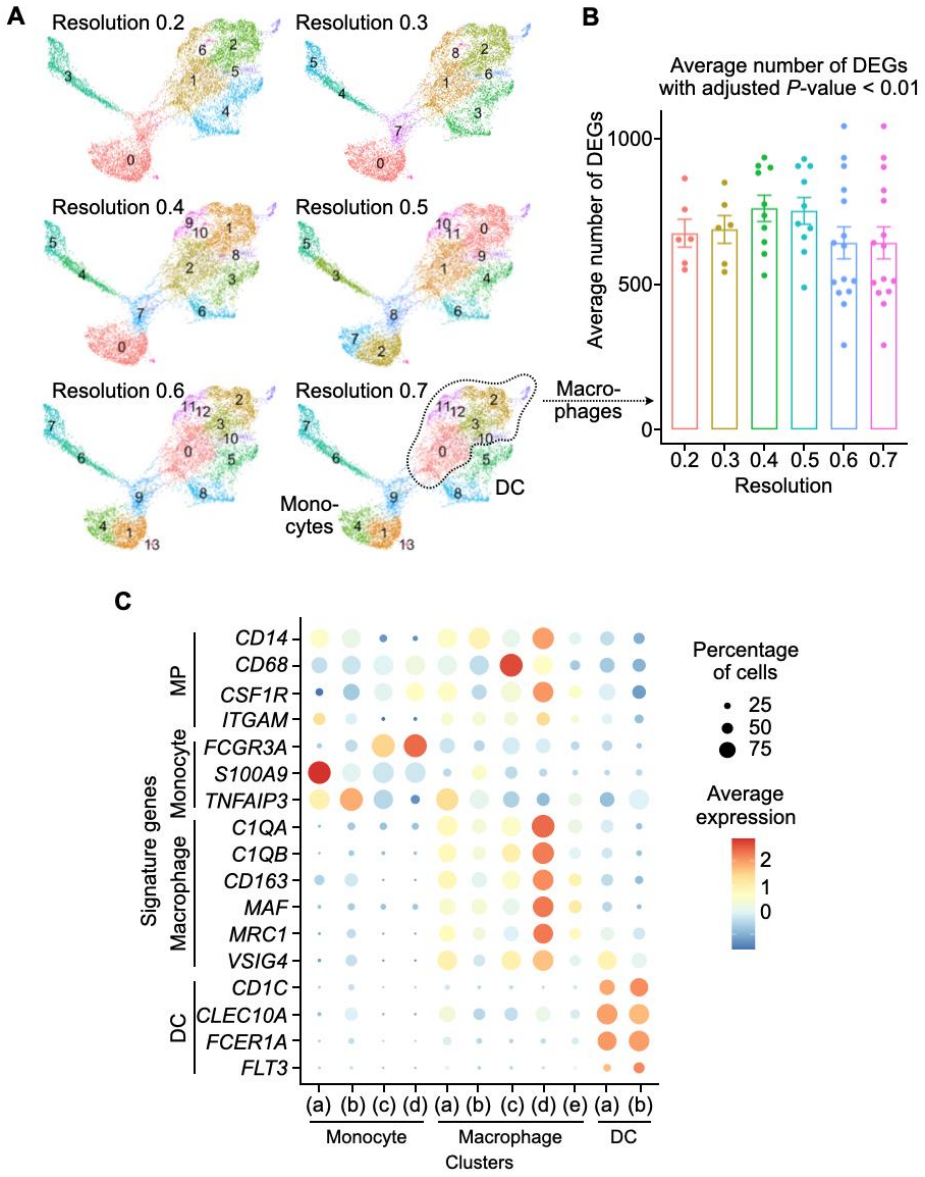

Fig. S5. **Resolution selection maximizing transcriptional changes between macrophage subsets.** (**A**) UMAP plots at indicated resolutions. (**B**) Average number of significant DEGs (with adjusted *P*-values < 0.01) between pairs of macrophage subclusters for resolutions ranging from 0.2 to 0.7. Bar graph data are means ± SEM with individual values for data distribution. (**C**) Dot plot identifying the MP/DC clusters by signature gene expression. Color denotes *z*-score of average gene expression (red: high; blue: low) and circle size indicates percentage of cells expressing the gene.

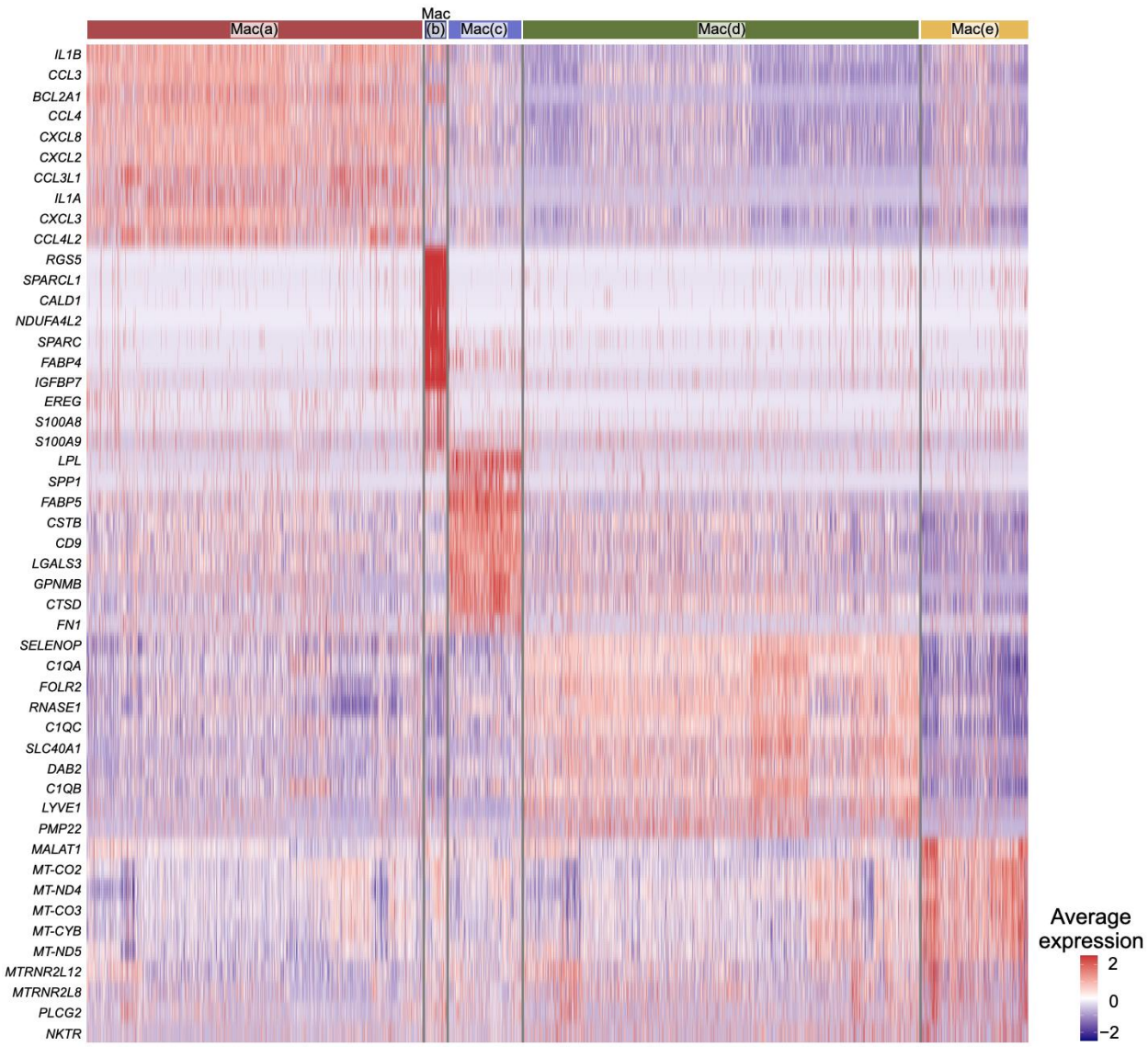

Fig. S6. Transcriptional signatures of the human macrophage clusters. Heatmap depicting the 10 most upregulated genes in each of the five macrophage clusters. These DEGs were obtained with Seurat's FindAllMarkers function comparing a subcluster against all other macrophages. The rows show the 10 genes with the highest fold changes for each cluster. Each column represents a cell.

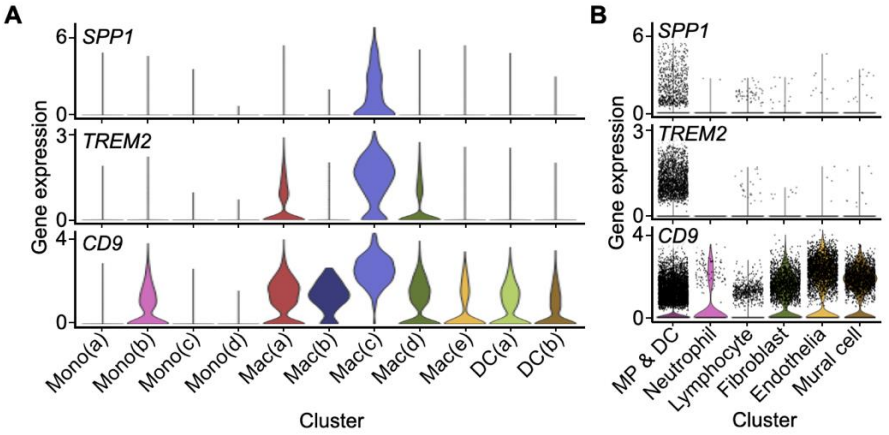

Fig. S7. *SPP1* expression in human non-cardiomyocytes. (**A**) Violin plots of indicated gene expression levels (represented by log-transformed normalized counts) across monocyte, macrophage and DC clusters. (**B**) Violin plots of indicated gene expression levels (represented by log-transformed normalized counts) across all major non-CM clusters.

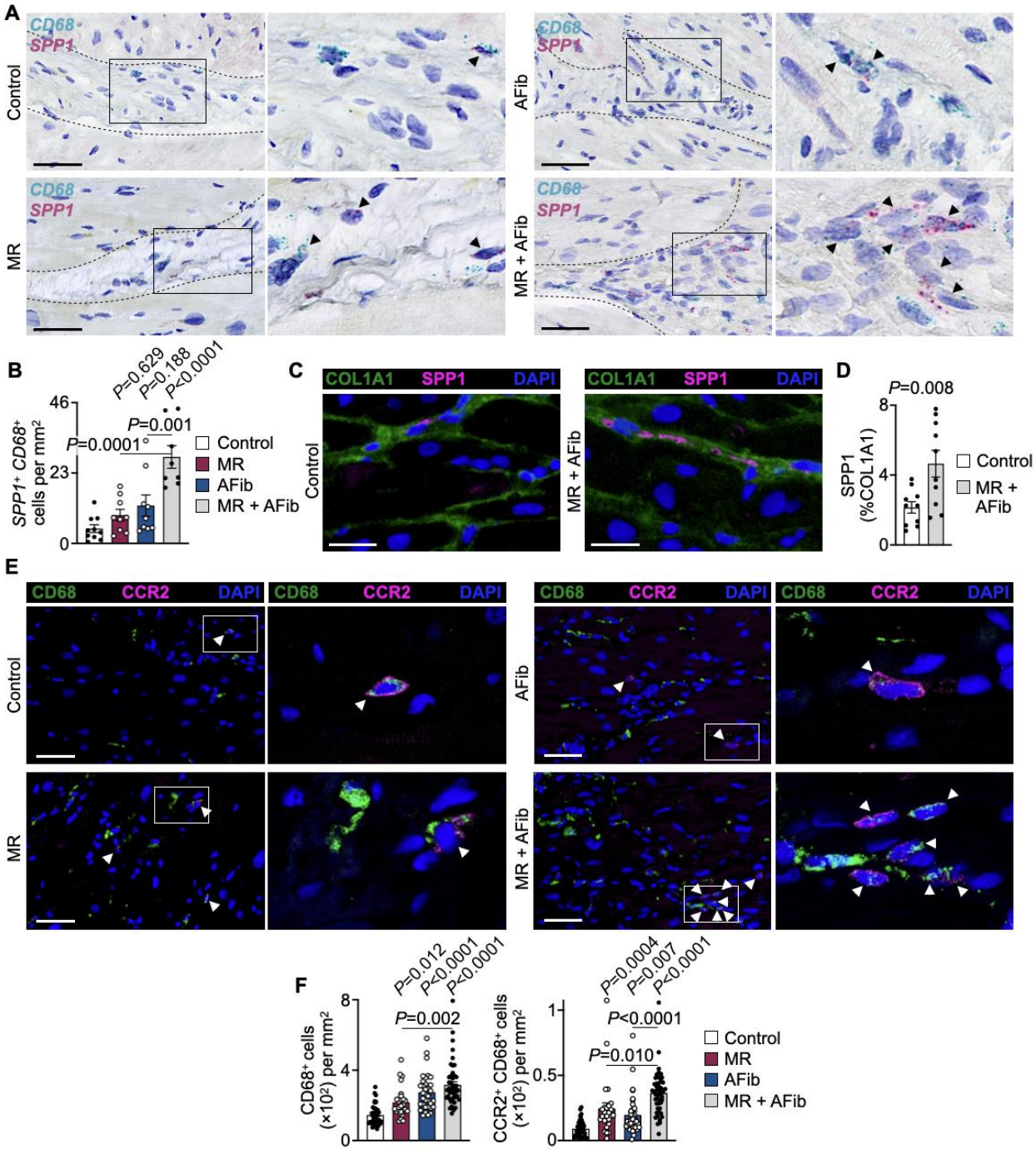

Fig. S8. *SPP1*-producing and CCR2$^+$ macrophages in human atrial disease. (**A**) In situ staining of *SPP1* (red) and *CD68* (green) mRNA on human left atrial tissue from controls, and "MR only", "AFib only" and "AFib with MR" patients. The area demarcated by dashed lines in representative images denotes a collagen-rich area. Higher magnification of the squared area is shown on the right. Arrowheads indicate *SPP1*$^+$*CD68*$^+$ macrophages and scale bars represent 50 µm. (**B**) Bar graph shows *SPP1*$^+$*CD68*$^+$ macrophages as absolute number per mm^2. *n* = 8-10 per group, ANOVA followed by Tukey's multiple comparisons test, all *P*-values are compared with controls unless indicated differently. (**C**) Representative immunofluorescent staining of SPP1 (magenta), collagen 1A1 (COL1A1) (green)—an extracellular matrix protein produced by

fibroblasts—and DAPI (blue) on left atrial tissue from controls and AFib patients. Scale bars represent 25 µm. (**D**) Bar graph shows percentage of SPP1-positive staining per COL1A1-positive area in left atrial tissue from controls and AFib patients. *n* = 10 per group, two-tailed Student's *t* test. (**E**) Representative immunofluorescent staining of CD68 (green), CCR2 (magenta), and DAPI (blue) on left atrial tissue from 41 controls, and 26 "MR only", 34 "AFib only" and 48 "AFib with MR" patients. Higher magnification of the squared area is shown on the right; arrowheads indicate recruited $CCR2^+$ $CD68^+$ macrophages; scale bars represent 50 µm. (**F**) Bar graphs show total $CD68^+$ and recruited $CCR2^+$ $CD68^+$ macrophages as absolute number per mm^2. *n* = 26-48 per group, Kruskal–Wallis test followed by Dunn's multiple comparisons test. All *P*-values are compared with controls unless indicated differently. All bar graph data are means ± SEM with individual values for data distribution.

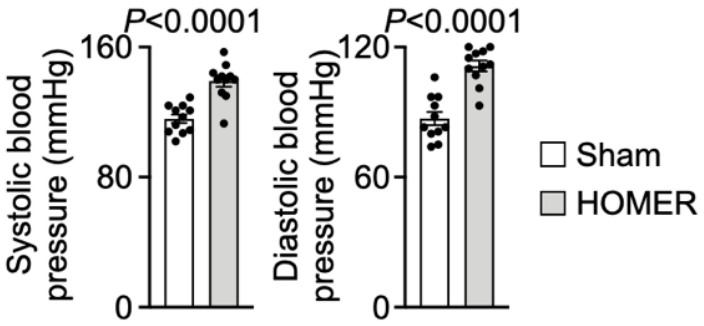

Fig. S9. Blood pressure measurements in HOMER mice. Systolic and diastolic blood pressure in sham and HOMER mice. Data are means ± SEM with individual values for data distribution. $n = 11$ per group from two independent experiments, two-tailed Student's *t* test.

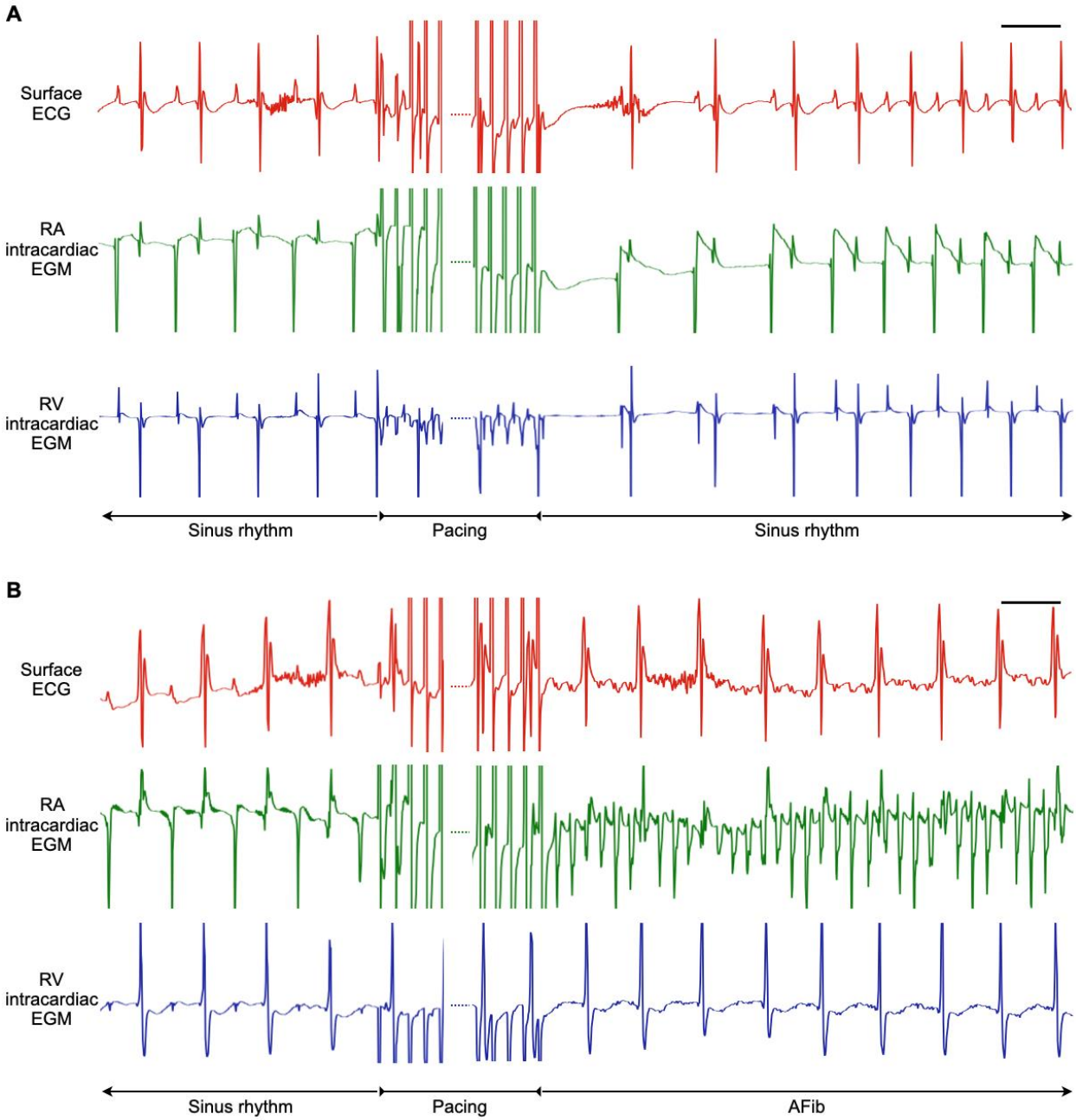

Fig. S10. ECG recordings obtained during invasive EP studies. Representative surface ECG and right atrial (RA) and right ventricular (RV) intracardiac electrograms (EGMs) during an invasive EP study in (**A**) a sham control mouse showing sinus rhythm and (**B**) a HOMER mouse showing AFib after rapid intracardiac pacing. Scale bars represent 100 ms.

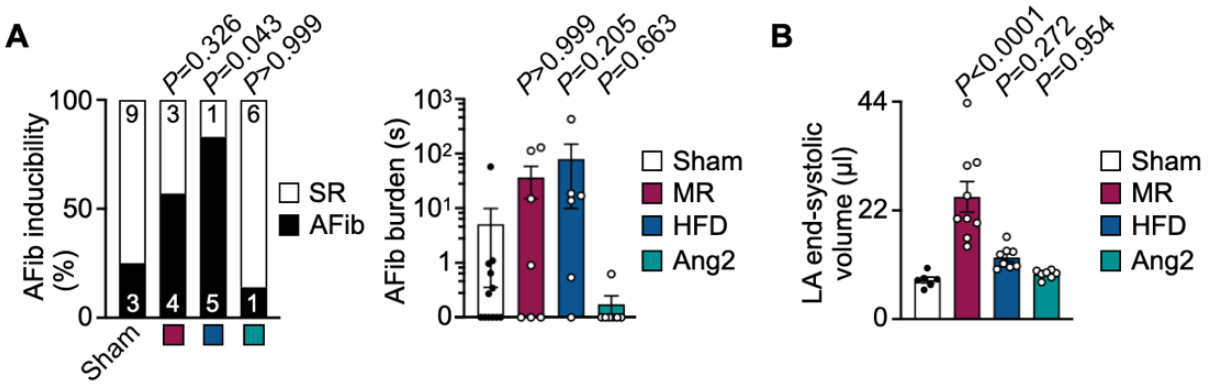

Fig. S11. Individual contribution of HOMER components to atrial disease. (**A**) EP study of AFib inducibility and burden in sham mice and mice exposed to MR, HFD or Ang2 infusion. *n* = 6-12 per group from two independent experiments. Left, two-sided Fisher's exact test; right, Kruskal–Wallis test followed by Dunn's multiple comparisons test. All *P*-values are compared with sham mice. (**B**) Cardiac MRI was used to quantify atrial size in sham mice and mice exposed to single components. *n* = 6-9 per group from two independent experiments, ANOVA followed by Dunnett's multiple comparisons test, all *P*-values are compared with sham mice. All bar graph data are means ± SEM with individual values for data distribution.

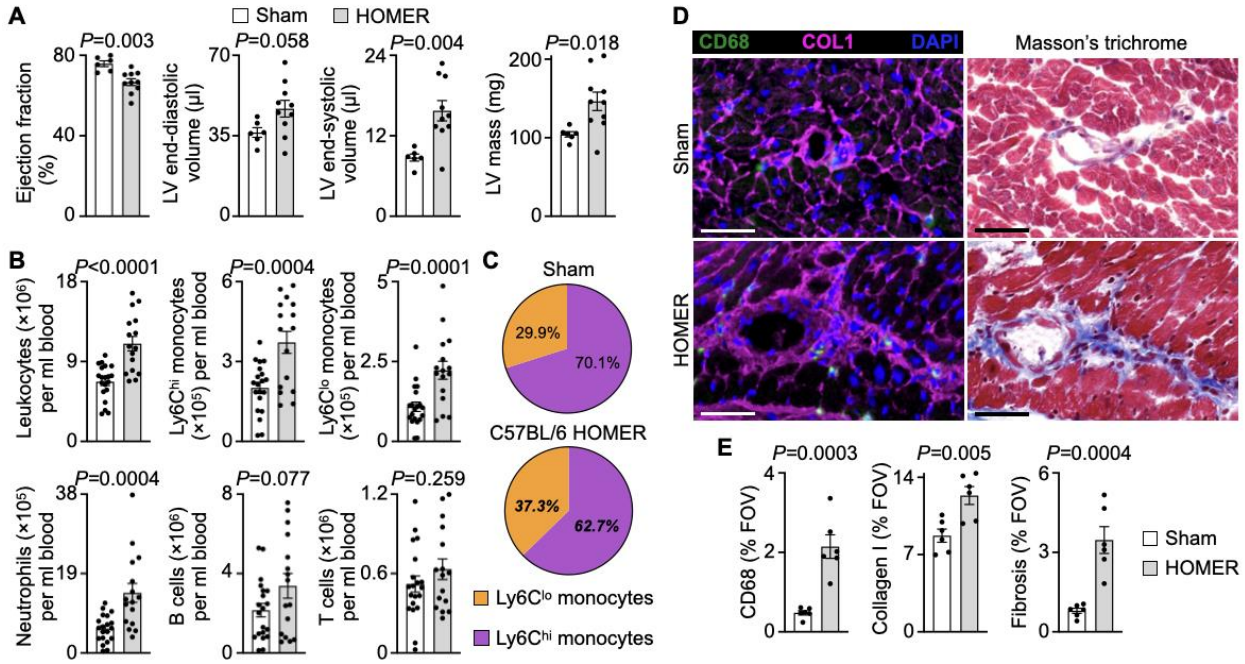

Fig. S12. Characterization of HOMER mouse model. (**A**) Cardiac MRI evaluation of left ventricular (LV) function, volumes and mass in sham and HOMER mice. *n* = 6-10 per group from two independent experiments, two-tailed Student's *t* test. (**B**) Flow cytometric quantification of leukocytes, monocytes, neutrophils and lymphocytes in blood from sham and HOMER mice. *n* = 16-20 per group from three independent experiments, two-tailed Student's *t* test. (**C**) Pie charts indicating the percentage of Ly6C^{lo} (orange) and Ly6C^{hi} (purple) monocytes in blood from sham and HOMER mice. Data are means. *n* = 16-17 per group from three independent experiments, two-tailed Mann–Whitney test, bold and italicized percentages denote *P*<0.01 compared with sham. (**D**) Representative immunofluorescent staining of macrophages (CD68) (green), collagen deposition (COL1) (magenta), and nuclei (DAPI) (blue) and histological staining of fibrosis (Masson's trichrome staining) in left atrial tissue from sham and HOMER mice. Scale bars represent 50 µm. (**E**) Quantification of CD68^{+}, COL1^{+} and fibrotic area in left atrial tissue from sham and HOMER mice. Bar graphs show percentage of positive staining per field of view (FOV). *n* = 6 per group from two independent experiments, two-tailed Student's *t* test. All bar graph data are means ± SEM with individual values for data distribution.

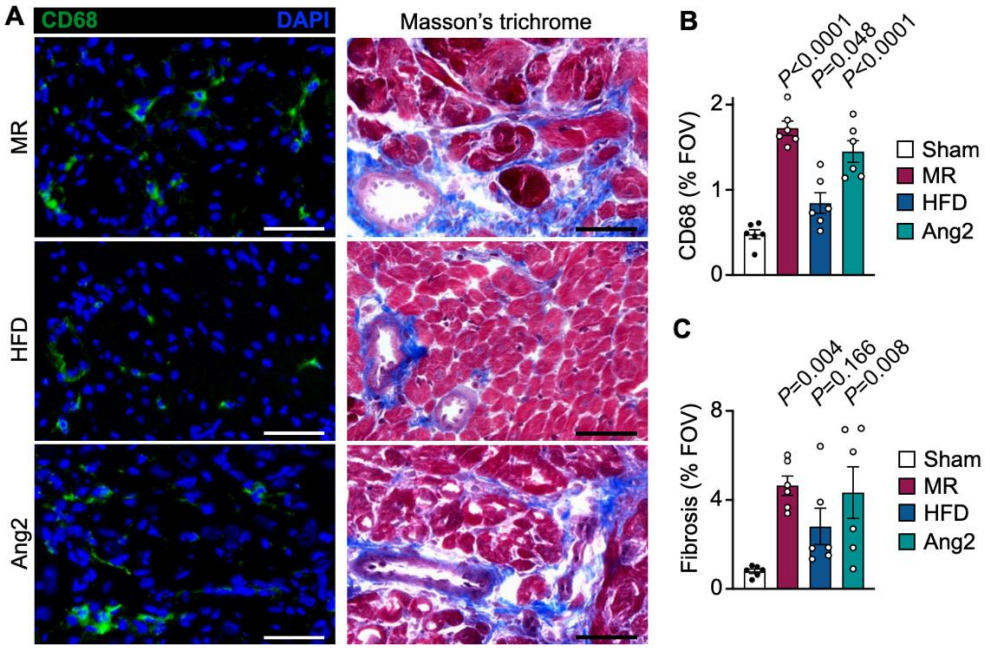

Fig. S13. Contribution of single HOMER components to macrophage expansion and atrial fibrosis. (**A**) Representative immunofluorescent staining of macrophages (CD68) (green) and nuclei (DAPI) (blue) and histological staining of fibrosis (Masson's trichrome staining) in left atrial tissue from sham mice and mice exposed to single conditions. Scale bars represent 50 μm. (**B** and **C**) Quantification of $CD68^+$ (B) and fibrotic (C) area in left atria from sham mice and mice exposed to single conditions. Bar graphs show percentage of positive staining per FOV. *n* = 6 per group from two independent experiments, ANOVA followed by Dunnett's multiple comparisons test, all *P*-values are compared with sham mice. All bar graph data are means ± SEM with individual values for data distribution.

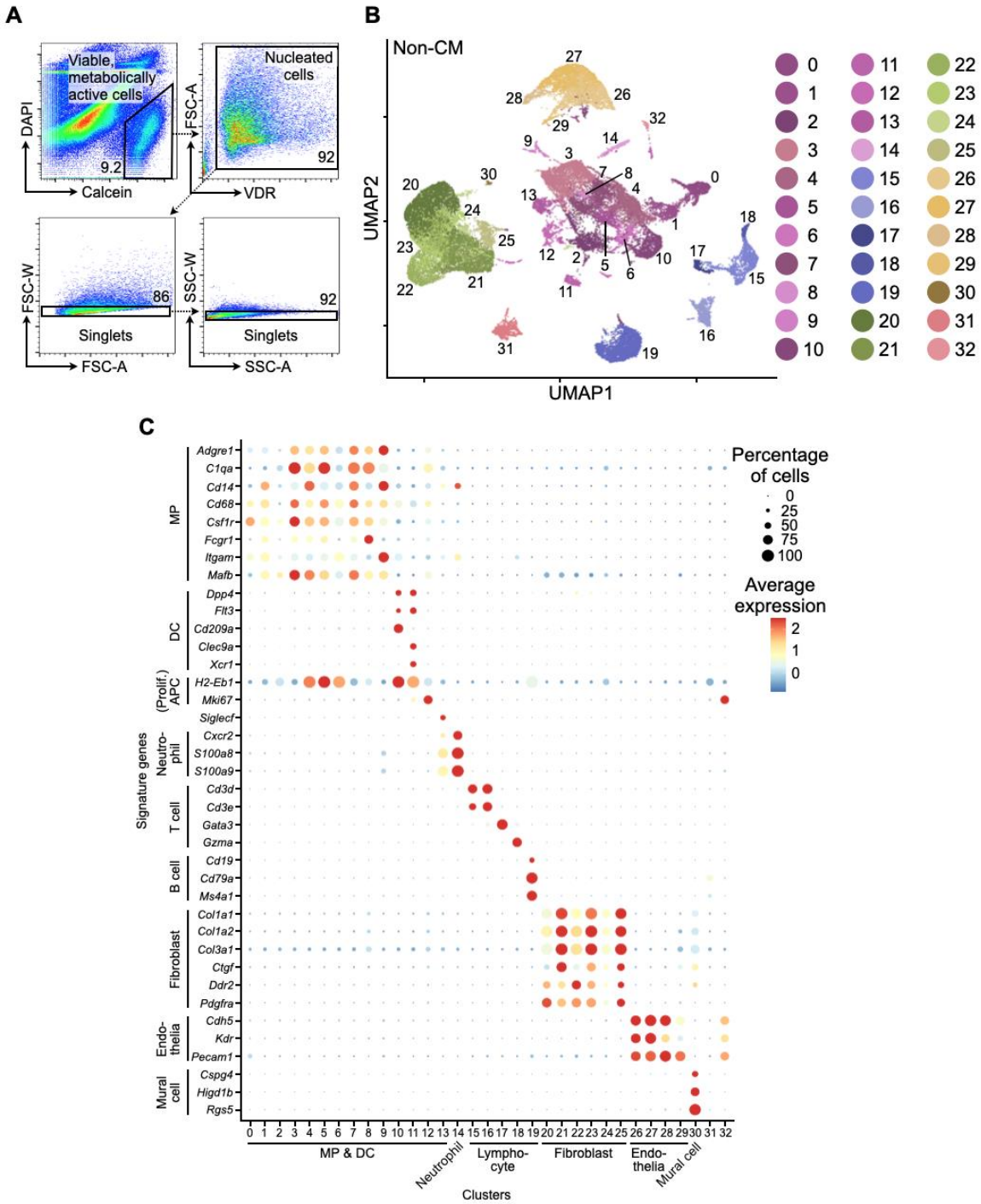

Fig. S14. Isolating and annotating mouse left atrial non-cardiomyocytes. (**A**) Representative plots of the flow cytometry gating strategy for isolating single, viable non-CM from mouse left atrial tissues. (**B**) Clustering of 40,112 non-CM from left atrial tissues of four sham and four HOMER mice. (**C**) Dot plot annotating non-CM clusters by signature gene expression. Color denotes *z*-score of average gene expression (red: high; blue: low) and circle size indicates the percentage of cells expressing the gene.

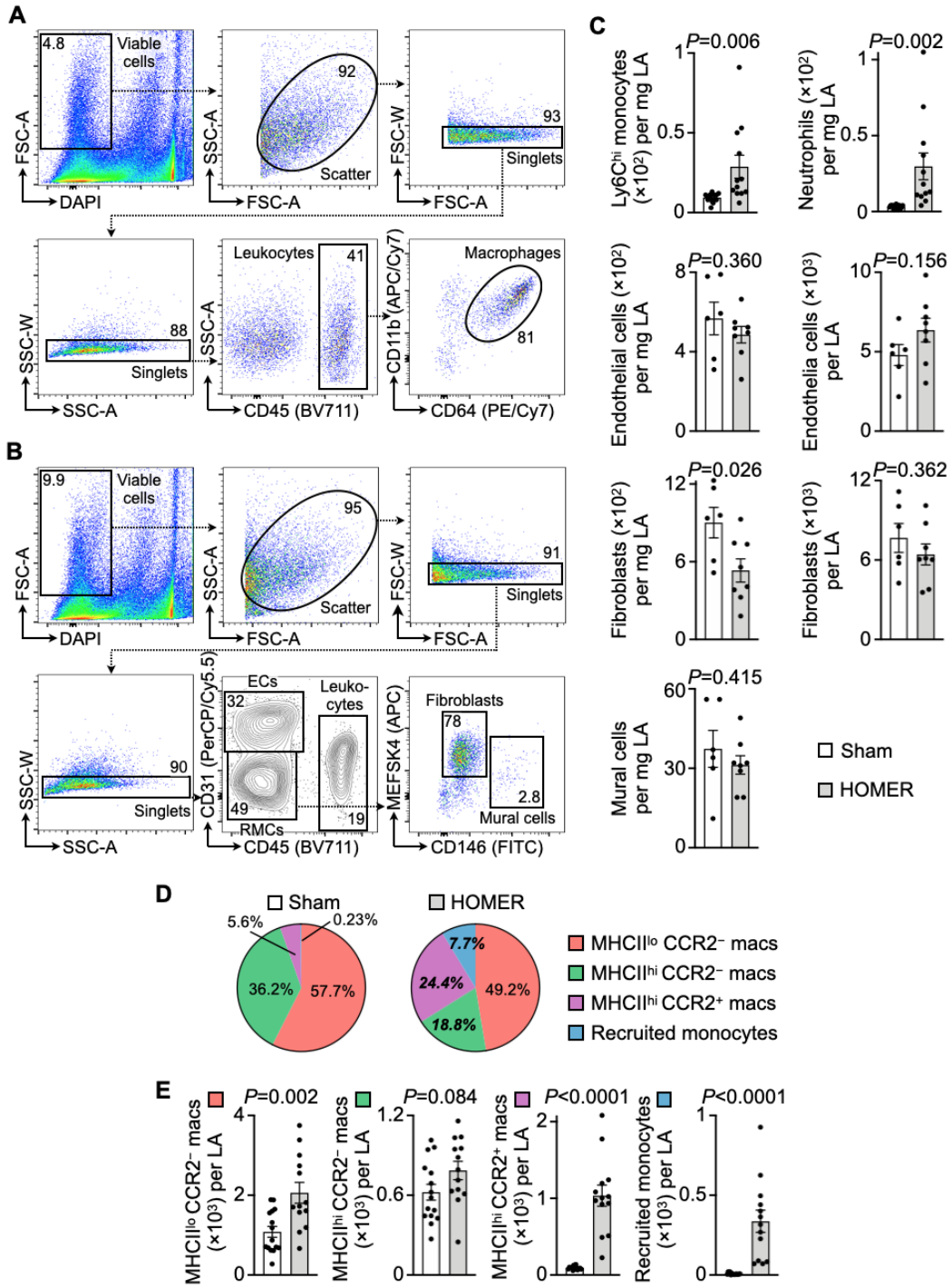

Fig. S15. Quantifying left atrial non-cardiomyocytes in HOMER mice. (**A**) Flow cytometry gating strategy to quantify cardiac macrophages in left atrial tissue. (**B**) Flow cytometry gating strategy to quantify cardiac endothelial cells (ECs), fibroblasts, and mural cells. RMCs: resident mesenchymal cells. (**C**) Flow cytometry to quantify left atrial Ly6C^{hi} monocytes, neutrophils, endothelial cells, fibroblasts, and mural cells in sham and HOMER mice. Ly6C^{hi} monocytes and neutrophils: 15 sham and 12 HOMER mice from three independent experiments; endothelial cells, fibroblasts and mural cells: 6 sham and 8 HOMER mice from two independent experiments; two-tailed Student's *t* test. (**D**) Pie charts indicating the percentage of

$MHCII^{lo}CCR2^{-}$ (coral), $MHCII^{hi}CCR2^{-}$ (green), $MHCII^{hi}CCR2^{+}$ (purple) macrophages, and recruited monocytes (blue) in left atrial tissue from sham and HOMER mice. Data are means. n = 13-15 per group from three independent experiments, two-tailed Student's t test, bold and italicized percentages denote $P<0.001$ compared with sham. (**E**) Absolute macrophage subset numbers per left atrial tissue from sham and HOMER mice. n = 13-15 per group from three independent experiments, two-tailed Student's t test. All bar graph data are means ± SEM with individual values for data distribution.

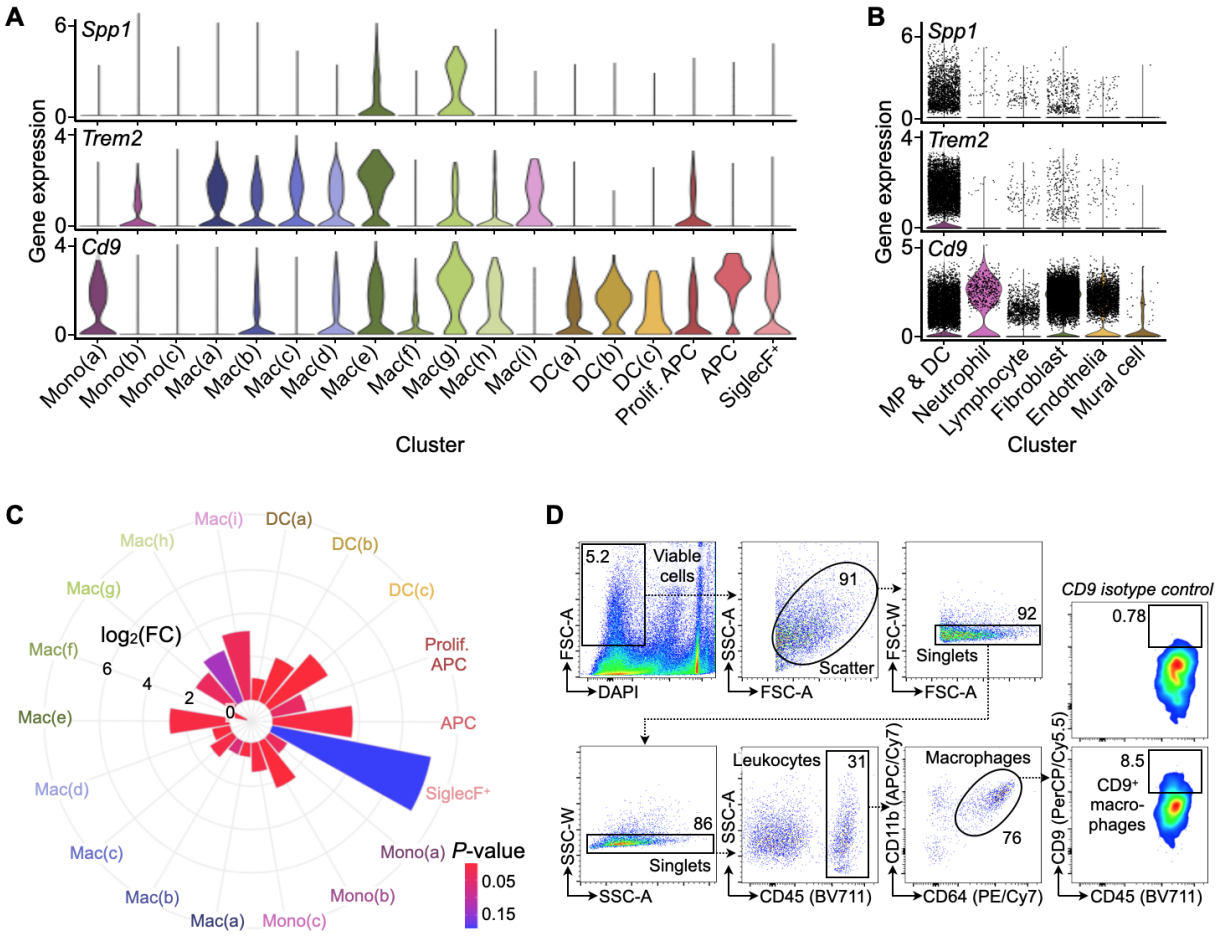

Fig. S16. *Spp1* expression in non-cardiomyocytes of the mouse atria. (**A**) Violin plots of indicated gene expression levels (represented by log-transformed normalized counts) across MP/DC subclusters. (**B**) Violin plots of indicated gene expression levels (represented by log-transformed normalized counts) across all major non-CM clusters. (**C**) Circular plot showing the difference in abundance of cells belonging to MP/DC subclusters between four HOMER and four sham mice. Pie size indicates $\log_2$-fold changes and color (blue: high; red: low) indicates the *P*-value (two-tailed Student's *t* test). (**D**) Flow cytometry gating strategy to quantify cardiac $CD9^+$ macrophages in left atrial tissue. Gates were set using a CD9 isotype control antibody.

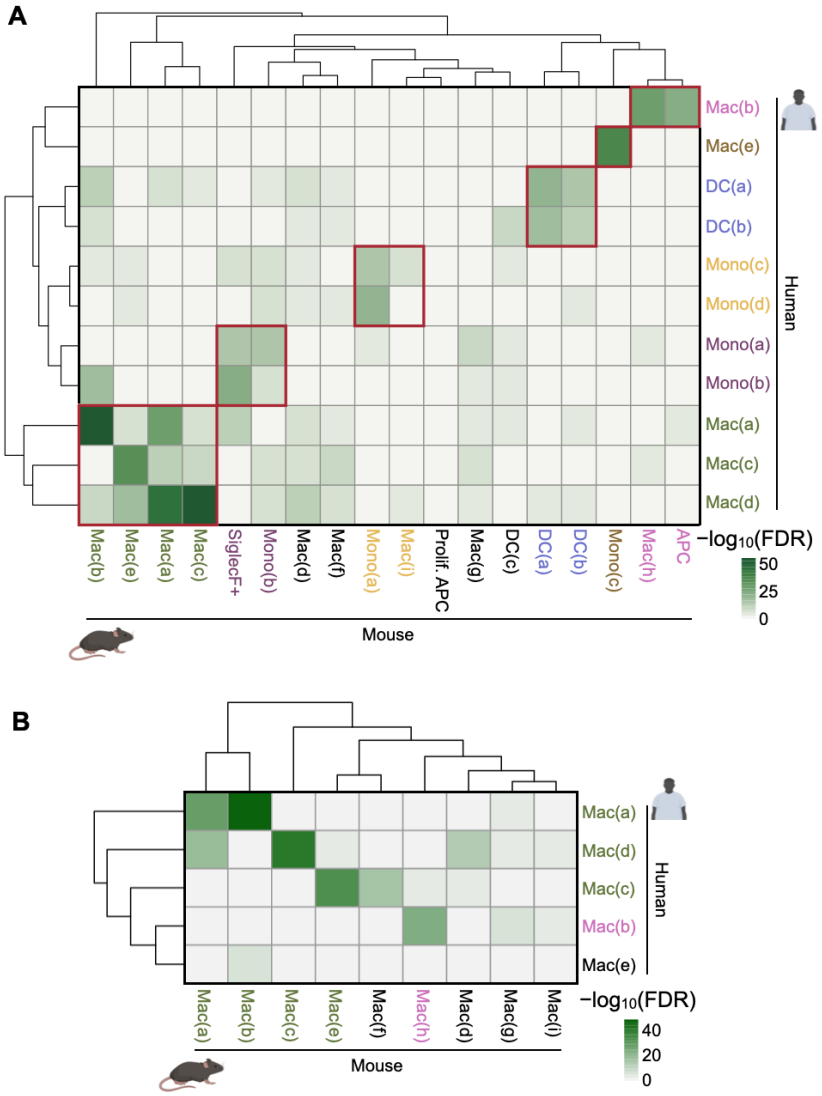

Fig. S17. Correlation of atrial myeloid cell phenotypes between human patients and mice. (**A**) Heatmap comparing human and mouse MP/DC subclusters using their top 100 DEGs compared to all other MP/DC subclusters. Only genes expressed in both species were included. The significance of the gene overlap between human and mouse clusters was obtained by two-sided Fisher's exact test with multiple testing corrected by the Benjamini–Hochberg method. Color (green: high; white: low) represents the $-\log_{10}$(FDR). (**B**) Same as in (A), but here only considering macrophage subsets.

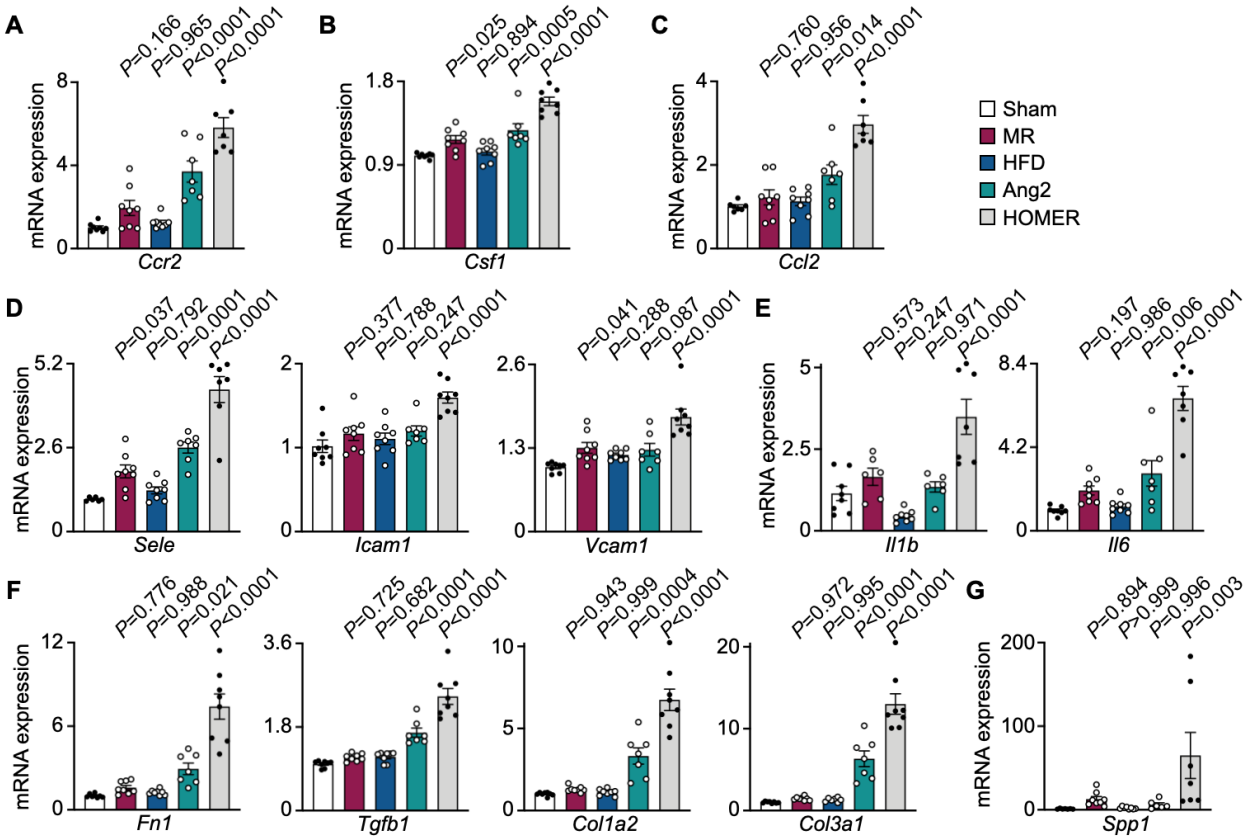

Fig. S18. Individual contribution of HOMER components to atrial expression of inflammatory and fibrotic genes. (**A** to **G**) Relative expression levels of inflammatory and fibrosis-related genes by qPCR in left atria from sham mice, mice exposed to single components and HOMER mice. Data are means ± SEM with individual values for data distribution. *n* = 6-8 per group from two independent experiments, ANOVA followed by Dunnett's multiple comparisons test, all *P*-values are compared with sham mice.

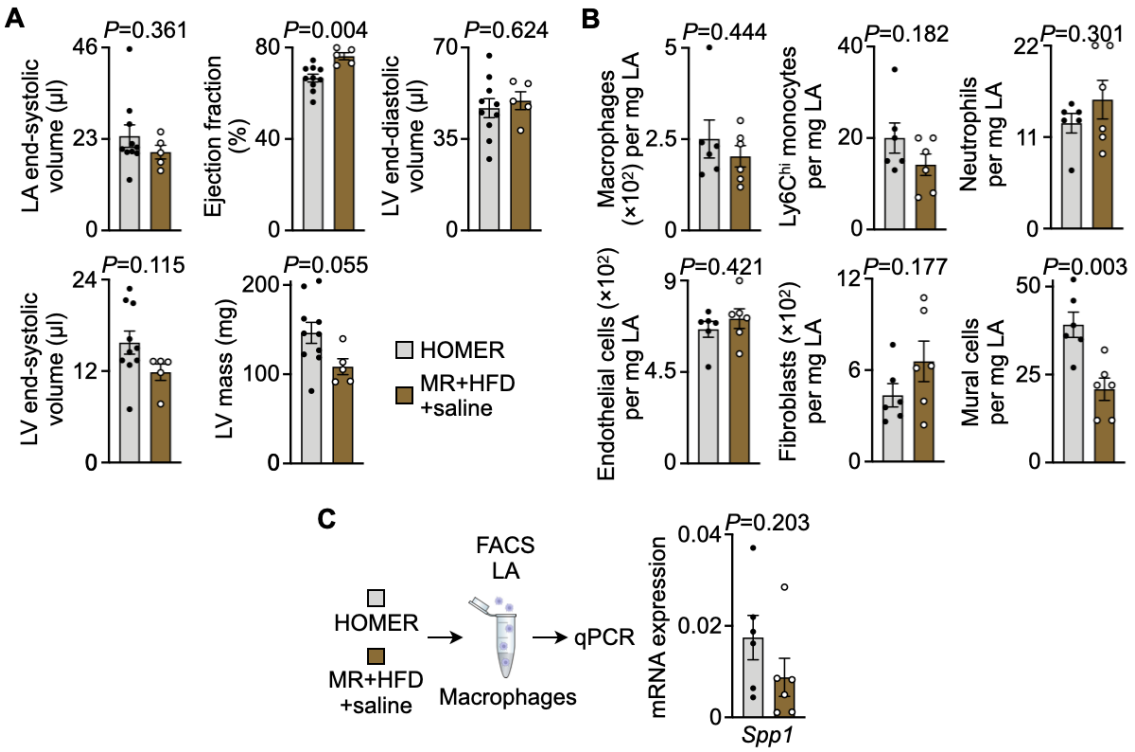

Fig. S19. Cardiac function and left atrial cellular frequencies in mice exposed to mitral regurgitation and high-fat diet only. (**A**) LA volume and LV function, volumes and mass in HOMER mice and mice exposed to MR and HFD only. *n* = 5-10 per group from two independent experiments, two-tailed Student's *t* test. (**B**) Flow cytometry to quantify left atrial macrophages, Ly6C^{hi} monocytes, neutrophils, endothelial cells, fibroblasts, and mural cells in HOMER mice and mice exposed to MR and HFD only. *n* = 6 per group from two independent experiments, two-tailed Student's *t* test. (**C**) Relative *Spp1* expression levels by qPCR in left atrial macrophages in HOMER mice and mice exposed to MR and HFD only. *n* = 6 per group from two independent experiments, two-tailed Student's *t* test. All bar graph data are means ± SEM with individual values for data distribution.

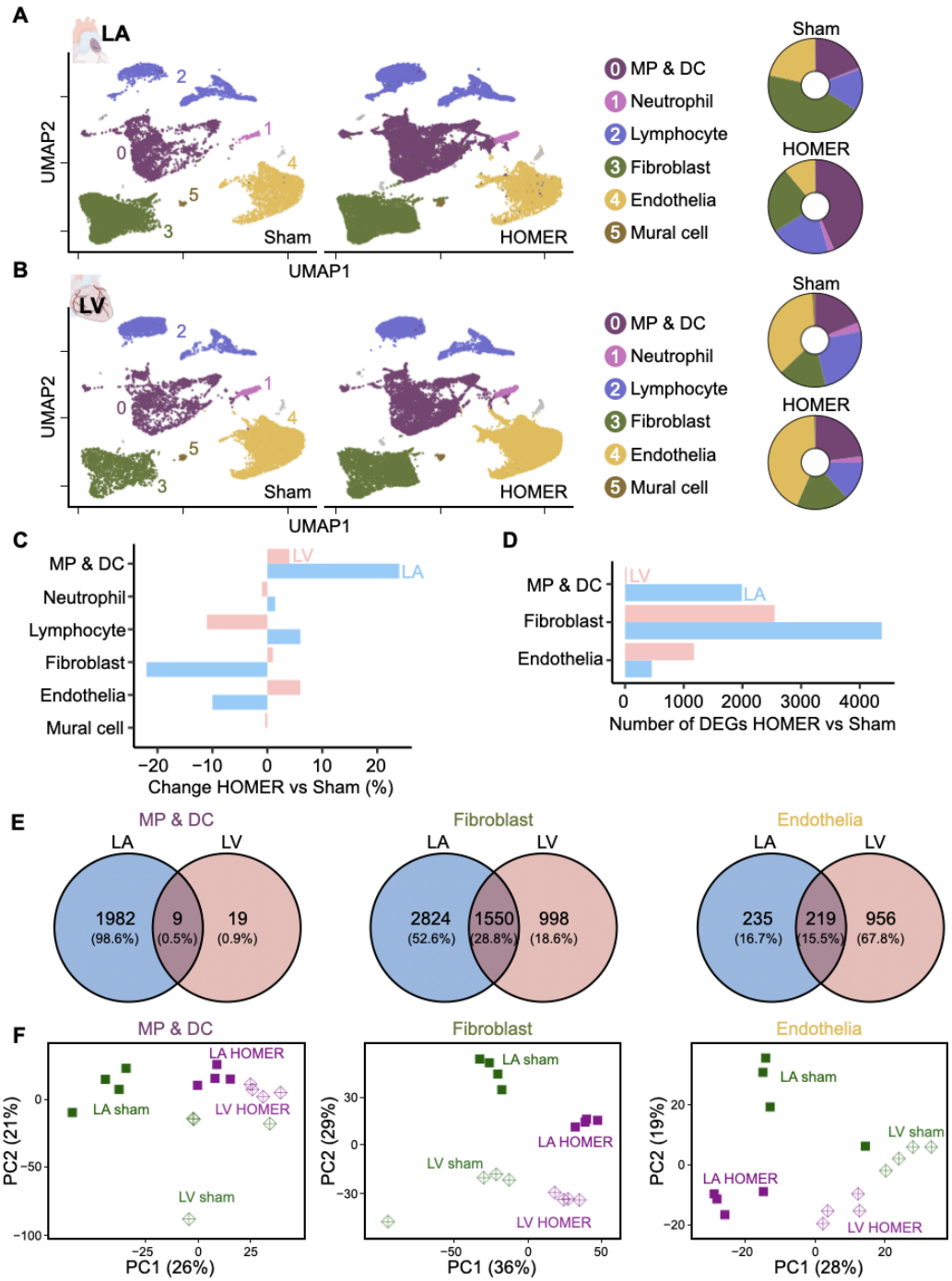

Fig. S20. Transcriptional comparison of left atria and ventricles from sham and HOMER mice. (**A** and **B**) Left, UMAP plots of cell clusters in left atria (LA, A) and left ventricles (LV, B) from four sham and four HOMER mice; right, cell population distributions in LA (A) and LV (B) from these mice. (**C**) HOMER-induced cell frequency changes comparing atria and ventricles. (**D**) Number of significant DEGs (with FDR<0.05) in MP/DC, fibroblast and endothelial subsets by pseudobulk differential analyses comparing the LA with LV. (**E**) Venn diagrams of these genes illustrating limited overlap of DEGs between atria and ventricles. (**F**) PCA plots for MP/DC, fibroblast and endothelial subsets of LA and LV samples from four sham and four HOMER mice.

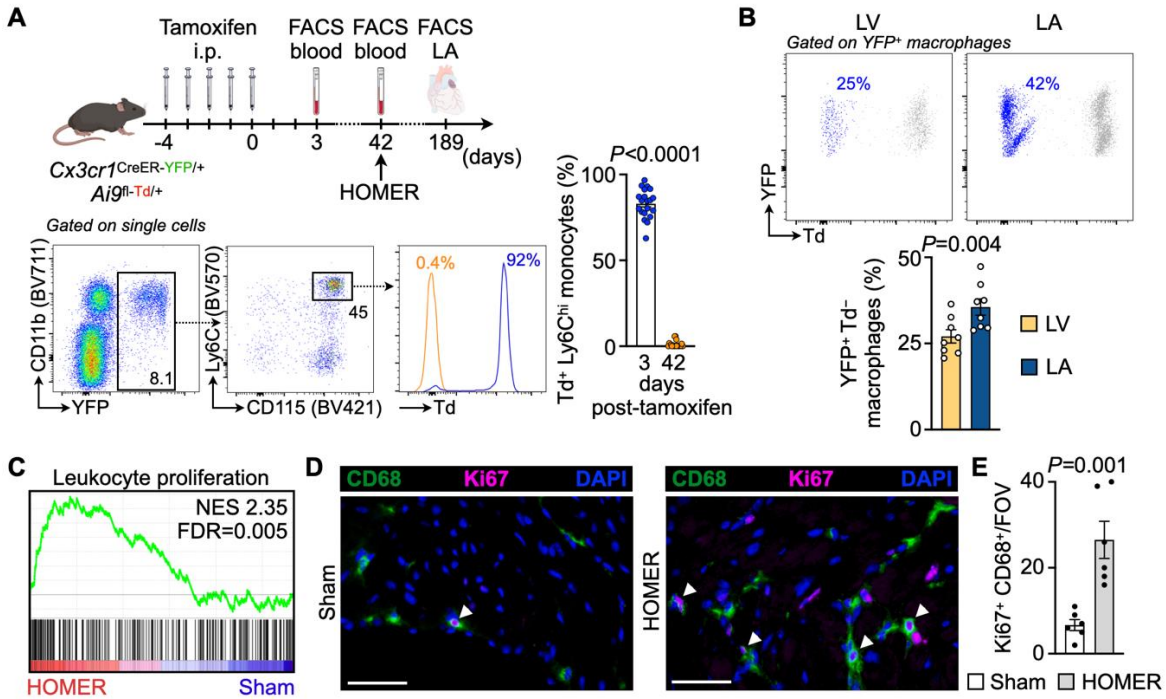

Fig. S21. Sources of left atrial macrophage expansion in HOMER mice. (**A**) Fate-mapping in *Cx3cr1*$^{CreER/+}$*Ai9*$^{fl/+}$ mice and quantification of tdTomato (Td) signal in YFP^{+}Ly6C^{hi} monocytes three (blue) and 42 (orange) days after final tamoxifen injection. *n* = 20 per group from two independent experiments, two-tailed Wilcoxon matched-pairs signed rank test. (**B**) Flow cytometric quantification of recruited (YFP^{+} Td$^{–}$) macrophages in LV (yellow) and LA (blue) from *Cx3cr1*$^{CreER/+}$*Ai9*$^{fl/+}$ sham mice. *n* = 8 per group from two independent experiments, two-tailed paired *t* test. (**C**) GSEA (gene set "leukocyte proliferation") of left atrial MP/DCs in four sham and four HOMER mice. (**D**) Representative immunofluorescent staining for the macrophage marker CD68 (green), proliferation marker Ki67 (magenta), and DAPI (blue) in left atria from sham and HOMER mice. Arrowheads indicate Ki67^{+} CD68^{+} macrophages and scale bars represent 50 µm. (**E**) Bar graph shows the number of Ki67^{+} CD68^{+} macrophages per FOV in left atria from sham and HOMER mice. *n* = 6 per group from two independent experiments, two-tailed Student's *t* test. All bar graph data are means ± SEM with individual values for data distribution.

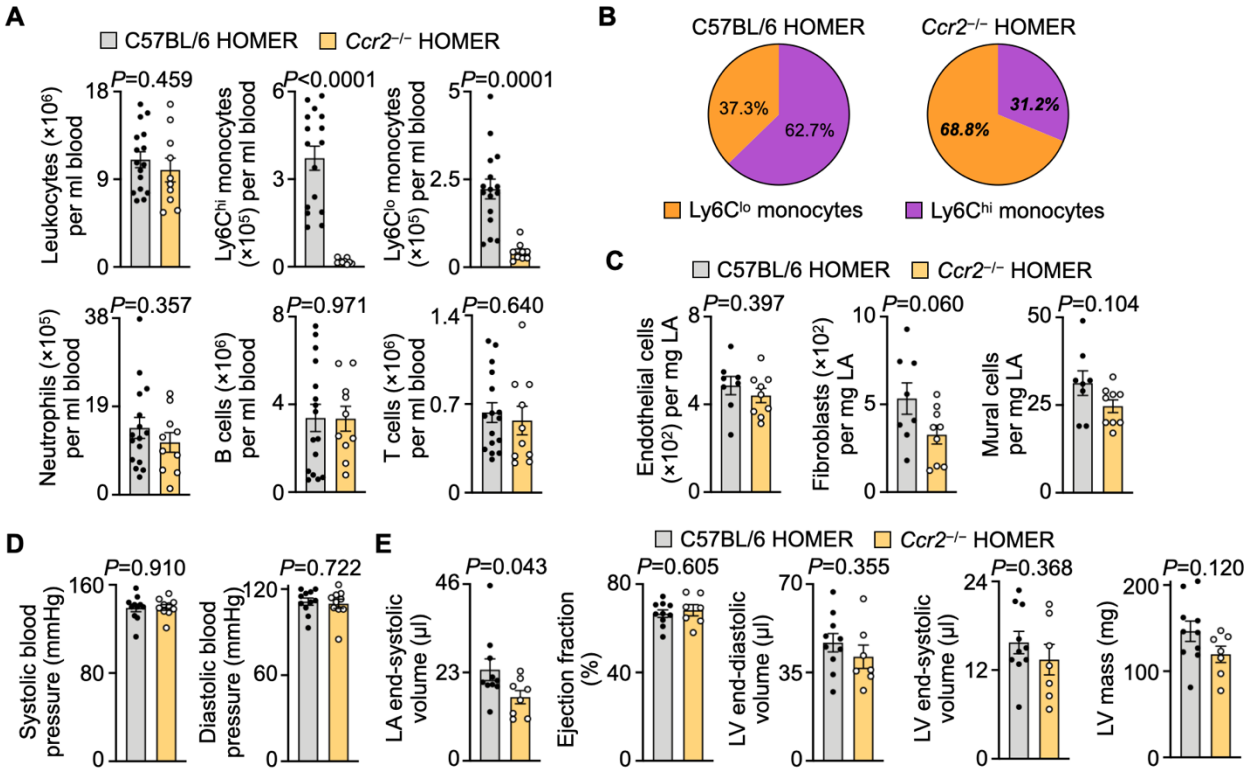

Fig. S22. Blood leukocytes, left atrial non-cardiomyocytes, blood pressure and cardiac function in *Ccr2*$^{-/-}$ HOMER mice. (**A**) Flow cytometric quantification of leukocytes, monocytes, neutrophils and lymphocytes in blood from C57BL/6 and *Ccr2*$^{-/-}$ HOMER mice. *n* = 9-16 per group from three independent experiments, two-tailed Student's *t* test. (**B**) Pie charts indicating the percentage of Ly6C^{lo} (orange) and Ly6C^{hi} (purple) monocytes in blood from C57BL/6 and *Ccr2*$^{-/-}$ HOMER mice. Data are means. *n* = 10-16 per group from three independent experiments, two-tailed Student's *t* test, bold and italicized percentages denote *P*<0.0001 compared with C57BL/6 HOMER mice. (**C**) Flow cytometric quantification of left atrial endothelial cells, fibroblasts and mural cells in C57BL/6 and *Ccr2*$^{-/-}$ HOMER mice. *n* = 8-9 per group from two independent experiments, two-tailed Student's *t* test. (**D**) Systolic and diastolic blood pressure in C57BL/6 and *Ccr2*$^{-/-}$ HOMER mice. *n* = 10-11 per group from two independent experiments, two-tailed Student's *t* test. (**E**) LA volume and LV function, volumes and mass in C57BL/6 and *Ccr2*$^{-/-}$ HOMER mice by cardiac MRI. *n* = 7-10 per group from two independent experiments; LA end-systolic volume: two-tailed Mann–Whitney test; other parameters: two-tailed Student's *t* test. All bar graph data are means ± SEM with individual values for data distribution.

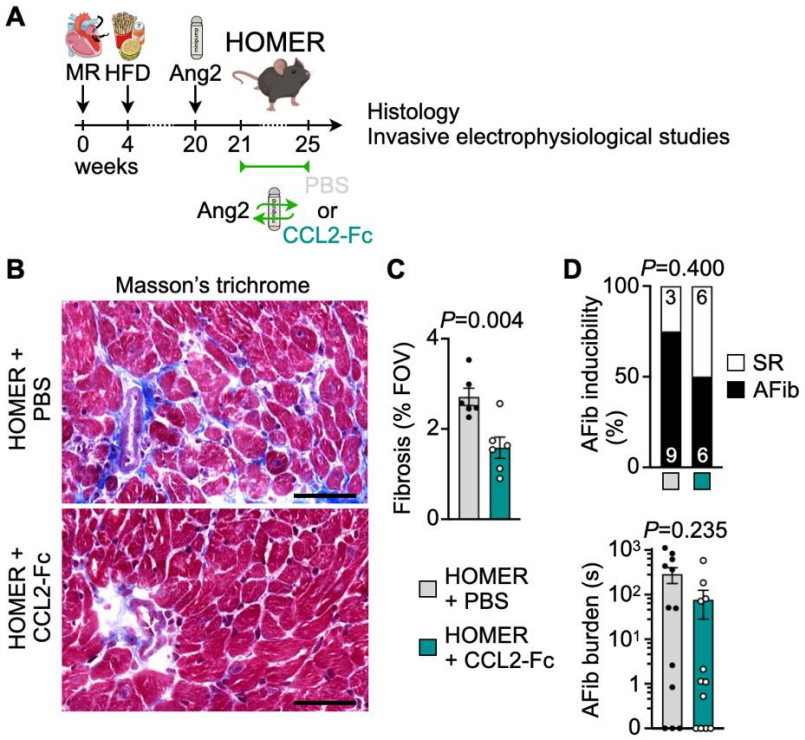

Fig. S23. CCR2 inhibition reduces atrial fibrosis. (**A**) Experimental outline. (**B**) Representative histological staining of fibrosis (Masson's trichrome staining) in left atrial tissue from PBS-treated HOMER mice and HOMER mice that were treated with a CCR2 inhibitor for 4 weeks. Scale bars represent 50 µm. (**C**) Quantification of fibrotic area in left atrial tissue from PBS-treated HOMER mice and HOMER mice that were treated with a CCR2 inhibitor for 4 weeks. Bar graph shows percentage of positive staining per FOV. n = 6 per group from two independent experiments, two-tailed Student's t test. (**D**) Invasive EP studies in PBS-treated HOMER mice and HOMER mice that were treated with a CCR2 inhibitor for 4 weeks. n = 12 per group from two independent experiments; AFib inducibility: two-sided Fisher's exact test; burden: two-tailed Mann–Whitney test. All bar graph data are means ± SEM with individual values for data distribution.

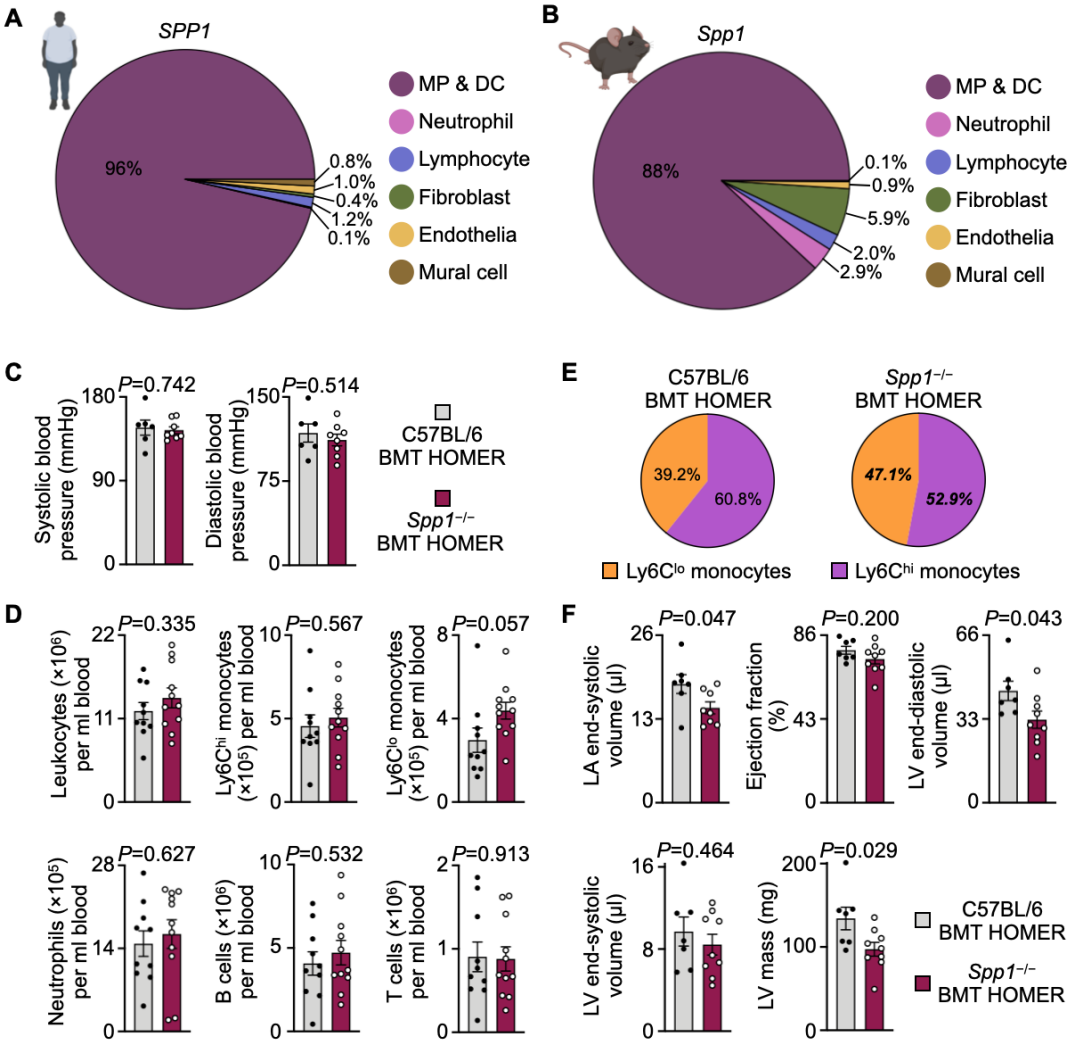

Fig. S24. *Spp1* deletion in HOMER mice. (**A** and **B**) Percentage of *SPP1* normalized counts across all major non-CM clusters in human (A) and mouse (B) left atrial tissues. (**C**) Systolic and diastolic blood pressure in C57BL/6 BMT HOMER and *Spp1*$^{-/-}$ BMT HOMER mice. *n* = 6-8 per group from two independent experiments, two-tailed Student's *t* test. (**D**) Flow cytometric quantification of leukocytes, monocytes, neutrophils and lymphocytes in blood from C57BL/6 BMT HOMER and *Spp1*$^{-/-}$ BMT HOMER mice. *n* = 10-11 per group from two independent experiments, two-tailed Student's *t* test. (**E**) Pie charts indicating the percentage of Ly6C^{lo} (orange) and Ly6C^{hi} (purple) monocytes in blood from C57BL/6 BMT HOMER and *Spp1*$^{-/-}$ BMT HOMER mice. Data are means. *n* = 10-11 per group from two independent experiments, two-tailed Student's *t* test, bold and italicized percentages denote $P<0.05$ compared with C57BL/6 BMT HOMER mice. (**F**) LA volume and LV function, volumes and mass in C57BL/6 BMT HOMER and *Spp1*$^{-/-}$ BMT HOMER mice by cardiac MRI. *n* = 7-9 per group from two independent experiments, two-tailed Student's *t* test. All bar graph data are means ± SEM with individual values for data distribution.

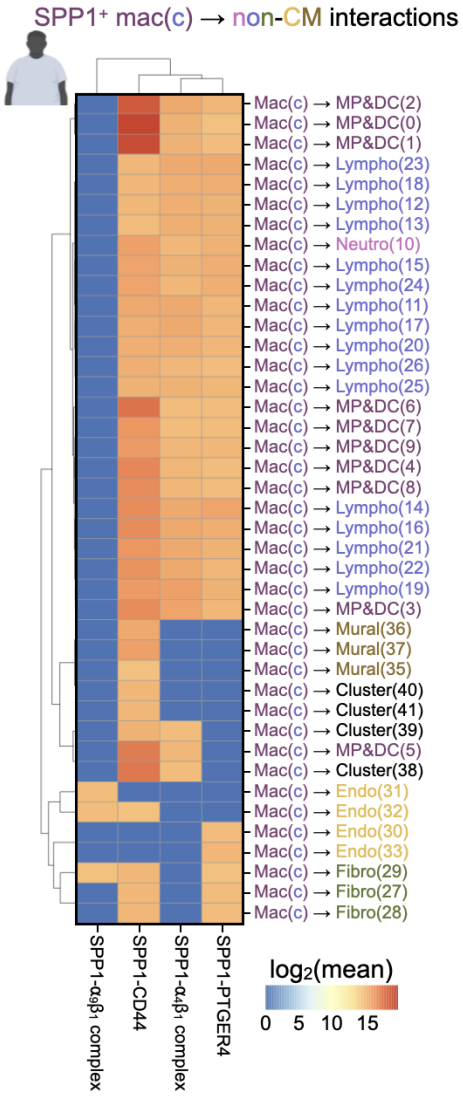

Fig. S25. SPP1 interactions in human atrial disease. Heatmap of SPP1–receptor interactions between SPP1$^+$ macrophages (mac(c)) and other non-CM in seven AFib patients. SPP1 and cognate receptors are shown on the *x*-axis. Cell populations that express *SPP1* and the receptor are shown on the *y*-axis and are color-coded according to the major cardiac cell types identified in Fig. 1B. Color of scale bar (red: high; blue: low) denotes average *SPP1* and receptor expression levels in their respective interacting subpopulations (represented by mean-normalized counts) if the enrichment of an interacting SPP1–receptor pair in the given interacting subpopulations was statistically significant (P<0.05). Non-significant interactions were assigned a value of 0.

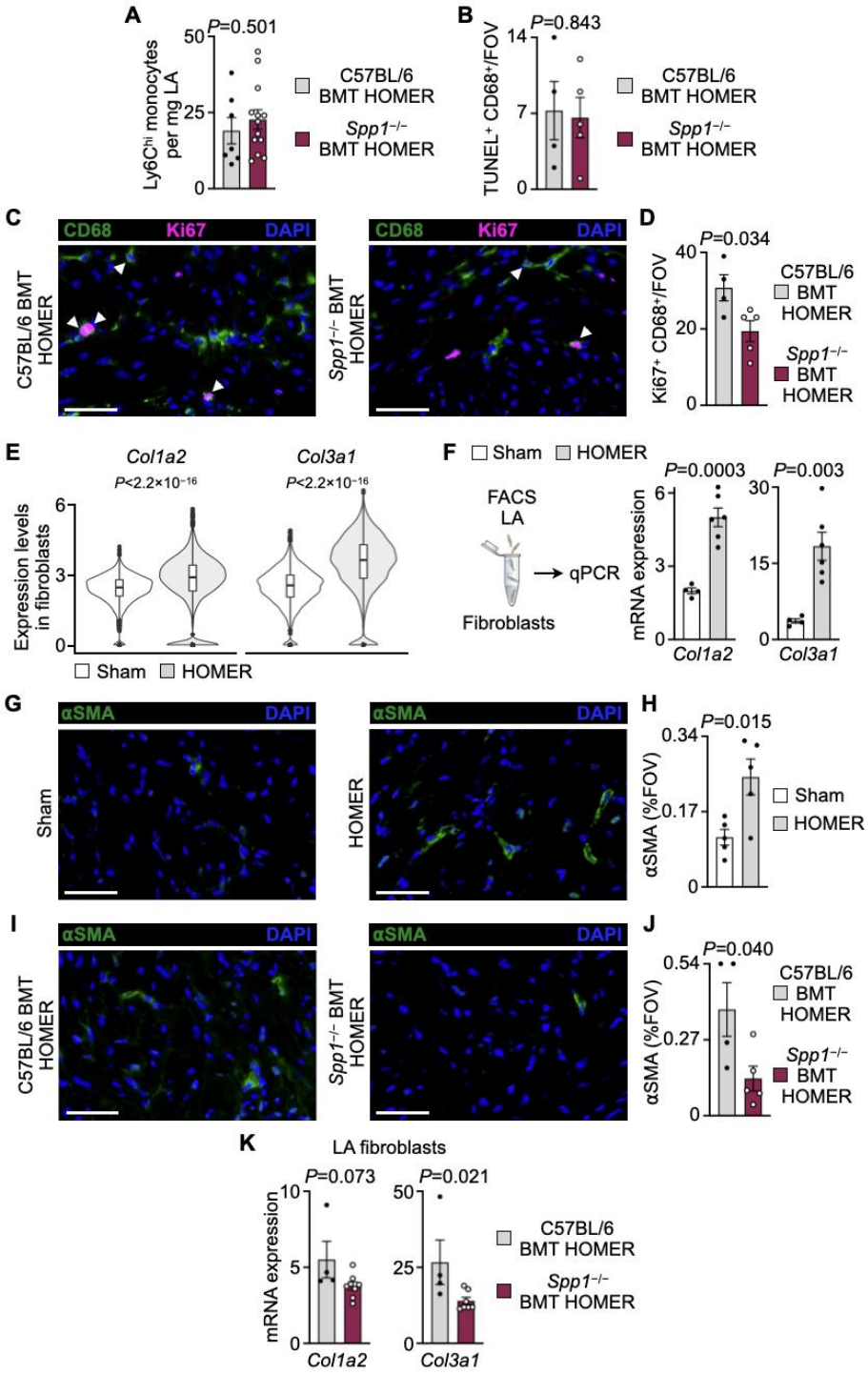

Fig. S26. *Spp1* deletion effects in HOMER atria. (**A**) Flow cytometric quantification of left atrial Ly6C^{hi} monocytes in C57BL/6 BMT HOMER and *Spp1*$^{-/-}$ BMT HOMER mice. n = 7-13 per group from two independent experiments, two-tailed Student's t test. (**B**) Immunofluorescent quantification of TUNEL^{+} macrophages in left atrial tissue obtained from C57BL/6 BMT HOMER and *Spp1*$^{-/-}$ BMT HOMER mice. Bar graph shows the number of TUNEL^{+} macrophages per FOV. n = 4-5 per group from two independent experiments, two-tailed Student's t test. (**C**) Representative immunofluorescent staining for the macrophage marker

CD68 (green), proliferation marker Ki67 (magenta), and DAPI (blue) in left atria from C57BL/6 BMT HOMER and *Spp1*$^{-/-}$ BMT HOMER mice. Arrowheads indicate Ki67^{+} CD68^{+} macrophages. (**D**) Bar graph shows the number of Ki67^{+} CD68^{+} macrophages per FOV in left atria from C57BL/6 BMT HOMER and *Spp1*$^{-/-}$ BMT HOMER mice. *n* = 4-5 per group from two independent experiments, two-tailed Student's *t* test. (**E**) Violin plots of indicated gene expression levels (represented by log-transformed normalized counts) in left atrial fibroblasts from four sham and four HOMER mice. *P*-values determined by two-sample Kolmogorov–Smirnov test. (**F**) Relative collagen expression levels by qPCR in FACS-purified left atrial fibroblasts from sham and HOMER mice. *n* = 4-6 per group, two-tailed Student's *t* test. (**G**) Representative immunofluorescent staining for αSMA (green) and DAPI (blue) in left atria from sham and HOMER mice. (**H**) Bar graph shows percentage of αSMA^{+} staining per FOV in left atria from sham and HOMER mice. *n* = 5 per group from two independent experiments, two-tailed Student's *t* test. (**I**) Representative immunofluorescent staining for αSMA (green) and DAPI (blue) in left atria from C57BL/6 BMT HOMER and *Spp1*$^{-/-}$ BMT HOMER mice. (**J**) Bar graph shows percentage of αSMA^{+} staining per FOV in left atria from C57BL/6 BMT HOMER and *Spp1*$^{-/-}$ BMT HOMER mice. *n* = 4-5 per group from two independent experiments, two-tailed Student's *t* test. (**K**) Relative collagen expression levels by qPCR in FACS-purified left atrial fibroblasts from C57BL/6 BMT HOMER and *Spp1*$^{-/-}$ BMT HOMER mice. *n* = 4-8 per group, two-tailed Mann–Whitney test. All bar graph data are means ± SEM with individual values for data distribution. All scale bars represent 50 μm.

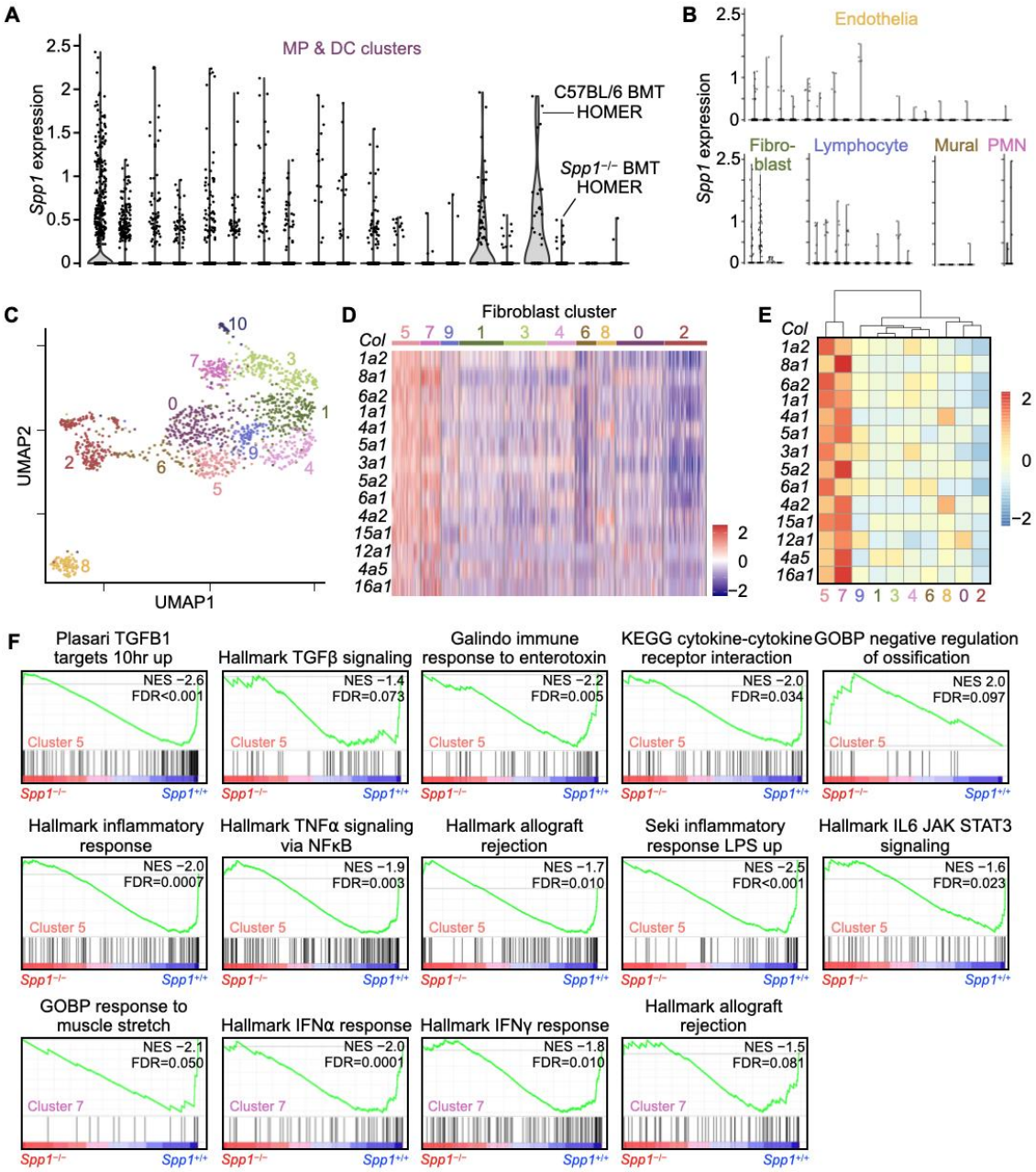

Fig. S27. SPP1 pathways in HOMER mice. (**A, B**) *Spp1* expression levels (represented by log-transformed normalized counts) across the macrophage clusters (A) and major cell types (B) in left atrial tissue from two C57BL/6 BMT HOMER and two *Spp1*$^{-/-}$ BMT HOMER mice. The *y*-axis was limited to 2.5 for data visualization. (**C**) UMAP plot of left atrial fibroblasts in two C57BL/6 BMT HOMER and two *Spp1*$^{-/-}$ BMT HOMER mice. Cluster 10 was omitted from further analyses shown in (D) and (E) due to its small size. (**D**) Heatmap depicting expression of collagen genes (represented by *z*-scores of the log-transformed normalized counts) in each of the 10 fibroblast clusters. The rows show the collagen genes and each column represents a cell. (**E**) Heatmap and hierarchical clustering of the fibroblast clusters according to the collagen gene expression levels (represented by *z*-scores of the average normalized counts). (**F**) GSEA results of fibroblast clusters 5 and 7 in two C57BL/6 BMT HOMER versus two *Spp1*$^{-/-}$ BMT HOMER mice.

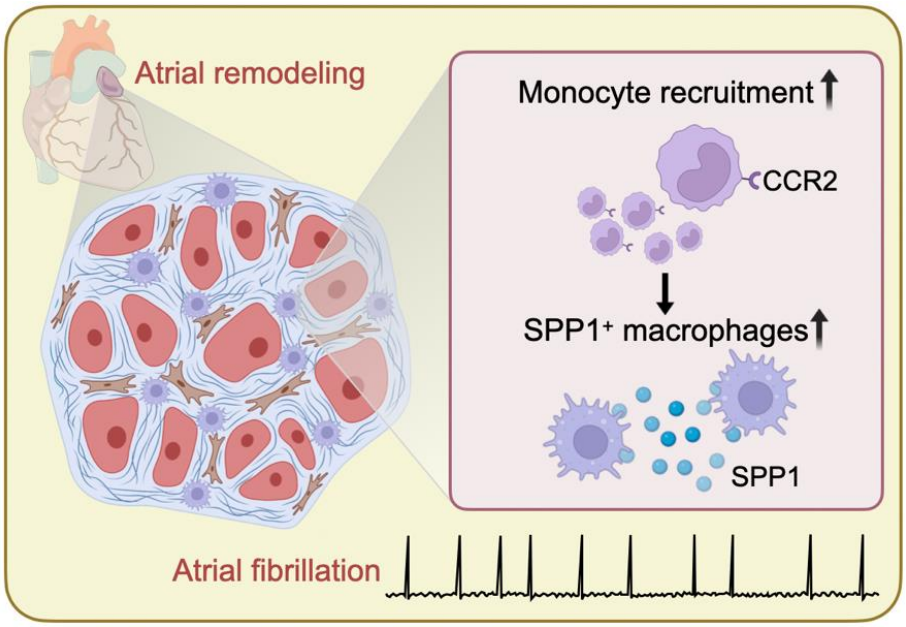

Fig. S28. Macrophage functions in atrial remodeling. In human and mouse atria, recruited macrophages upregulate SPP1 expression, which augments inflammation and fibrosis. Through these functions, macrophages contribute to the electrophysiological substrate of atrial fibrillation.

Table S1. Patient demographics and clinical information (scRNA-seq cohort).

	Control (*n* = 5)	**MR + AFib (*n* = 7)**
Age (years)	65±6	71±5
Sex (male/female)	5/0	5/2
Race (white/black or African American/Hispanic/n/a)	5/0/0/0	6/0/0/1
BMI (kg/m^2)	26±1	26±2
Hypertension (Y/N)	5/0	6/1
Diabetes (Y/N)	2/3	1/6
Hyperlipidemia (Y/N)	4/1	7/0
LVEF (%)	56±3	61±2
LA antero-posterior diameter (mm)	38±3 1 n/a	48±3
LA volume index (ml/m^2)	30±2	73±9 1 n/a
RA size (normal/dilated/n/a)	4/0/1	3/4/0

Data are means ± SEM. BMI, body mass index; LA, left atrial; LVEF, left ventricular ejection fraction; n/a, not available; RA, right atrial.

Table S2. Distribution of cell populations in human LA by scRNA-seq.

Cell type	Control (*n* = 5)	MR + AFib (*n* = 7)	*P*-value
MP & DC	15±2%	28±5%	**0.044**
Neutrophil	0.9±0.2%	1.2±0.2%	0.474
Lymphocyte	52±4%	54±6%	0.759
Fibroblast	9±2%	5±2%	0.271
Endothelia	15±3%	5±1%	**0.004**
Mural cell	8±1%	4±1%	**0.044**

Data are means ± SEM, two-tailed Student's *t* test. MP & DC, mononuclear phagocyte and dendritic cell.

Table S3. Patient demographics and clinical information (histology cohort).

	Control (*n* = 41)	**MR only (*n* = 26)**	**AFib only (*n* = 34)**	**MR + AFib (*n* = 48)**
Age (years)	67±2	64±2	72±2 1 n/a	71±1
Sex (male/female)	31/10	16/10	30/4	32/16
Race (white/black or African American/Hispanic/n/a)	39/0/1/0/1	26/0/0/0/0	30/3/0/1/0	47/1/0/0/0
AFib chronicity (paroxysmal/persistent or permanent)	-	-	16/17 1 n/a	10/38
Hypertension (Y/N)	30/11	19/7	31/3	33/15
Diabetes (Y/N)	15/26	3/23	9/25	5/43
Hyperlipidemia (Y/N)	25/16	12/14	21/12 1 n/a	20/27 1 n/a
LVEF (%)	58±1 2 n/a	53±2 2 n/a	53±2 1 n/a	52±1 4 n/a
Significant LA dilatation (Y/N)	4/34 3 n/a	12/10 4 n/a	13/18 3 n/a	36/7 5 n/a
Significant RA dilatation (Y/N)	5/33 3 n/a	3/19 4 n/a	7/19 8 n/a	25/13 10 n/a

Data are means ± SEM. LA, left atrial; LVEF, left ventricular ejection fraction; n/a, not available; RA, right atrial.

Table S4. General characteristics of sham and HOMER mice.

	Sham (*n* = 15)	**HOMER (*n* = 8)**	***P*-value**
Body weight (g)	29.8±1.0	39.7±3.1	**0.001**
Heart weight (mg)	146.8±3.2	201.5±9.3	**<0.0001**
LA weight (mg)	7.5±0.4	11.3±0.6	**<0.0001**
LV weight (mg)	68.8±2.0	91.8±1.7	**<0.0001**

Data are means ± SEM from two independent experiments, two-tailed Student's *t* test. LA, left atrial; LV, left ventricular.

Table S5. Distribution of cell populations in mouse LA by scRNA-seq.

Cell type	Sham (*n* = 4)	HOMER (*n* = 4)	*P*-value
MP & DC	19±2%	43±2%	**<0.0001**
Neutrophil	0.6±0.2%	2.0±0.4%	**0.031**
Lymphocyte	14±2%	18±4%	0.371
Fibroblast	44±5%	22±4%	**0.013**
Endothelia	21±8%	11±2%	0.226
Mural cell	0.2±0.1%	0.2±0.04%	0.957

Data are means ± SEM, two-tailed Student's *t* test. MP & DC, mononuclear phagocyte and dendritic cell.

Table S6. Distribution of cell populations in mouse LA and LV by scRNA-seq.

Cell type	Sham (*n* = 4)	HOMER (*n* = 4)	*P*-value
LA			
MP & DC	19±2%	43±2%	**<0.0001**
Neutrophil	0.6±0.2%	2.0±0.5%	**0.037**
Lymphocyte	14±2%	20±5%	0.277
Fibroblast	45±5%	23±4%	**0.013**
Endothelia	21±8%	11±2%	0.226
Mural cell	0.2±0.1%	0.2±0.05%	>0.999
LV			
MP & DC	19±4%	23±3%	0.518
Neutrophil	3.1±0.5%	2.1±0.4%	0.155
Lymphocyte	24±3%	13±4%	0.077
Fibroblast	17±6%	18±2%	0.852
Endothelia	36±5%	42±6%	0.441
Mural cell	0.9±0.1%	0.5±0.1%	**0.043**

Data are means ± SEM, two-tailed Student's *t* test. LA, left atria; LV, left ventricles; MP & DC, mononuclear phagocyte and dendritic cell.

Table S7. Electrophysiological parameters of sham and HOMER mice by in vivo EP study.

	Sham (*n* = 12)	**HOMER (*n* = 8)**	***P*-value**
Baseline characteristics			
BCL	119±3	124±5	0.304
PR interval	48±2	55±2	**0.017**
QRS interval	27±2	28±2	0.855
Atrial characteristic			
$AERP_{100ms}$	25±2	28±2	0.211
Sinus node function			
$SNRT_{100ms}$	157±10	157±14	0.995
$SNRT_{80ms}$	181±13	157±10	0.215
Atrioventricular node function			
$AVERP_{100ms}$	44±2	42±4	0.640
WCL	76±1	79±2	**0.038**
2:1 CL	55±1	57±1	0.437

Data are means ± SEM from two independent experiments, two-tailed Student's *t* test. 2:1 CL, 2:1 conduction cycle length; AERP, atrial effective refractory period; AVERP, atrioventricular node effective refractory period; BCL, basic cycle length; SNRT, sinus node recovery time; WCL, Wenckebach cycle length.

Table S8. Electrophysiological parameters of C57BL/6 and *Ccr2*$^{-/-}$ HOMER mice by in vivo EP study.

	C57BL/6 HOMER (*n* = 8)	*Ccr2*$^{-/-}$ HOMER (*n* = 9)	*P*-value
Baseline characteristics			
BCL	124±5	131±7	0.396
PR interval	55±2	55±3	0.923
QRS interval	28±2	30±2	0.378
Atrial characteristic			
$AERP_{100ms}$	28±2	32±4	0.376
Sinus node function			
$SNRT_{100ms}$	157±14	170±10	0.452
$SNRT_{80ms}$	157±10	175±6	0.137
Atrioventricular node function			
$AVERP_{100ms}$	42±4	53±6	0.104
WCL	79±2	83±2	0.195
2:1 CL	57±1	68±4	**0.022**

Data are means ± SEM from two independent experiments, two-tailed Student's *t* test. 2:1 CL, 2:1 conduction cycle length; AERP, atrial effective refractory period; AVERP, atrioventricular node effective refractory period; BCL, basic cycle length; SNRT, sinus node recovery time; WCL, Wenckebach cycle length.

Table S9. Electrophysiological parameters of C57BL/6 BMT and *Spp1*$^{-/-}$ BMT HOMER mice by in vivo EP study.

	C57BL/6 BMT HOMER (*n* = 13)	*Spp1*$^{-/-}$ BMT HOMER (*n* = 13)	*P*-value
Baseline characteristics			
BCL	134±5	126±4	0.262
PR interval	59±3	59±3	>0.999
QRS interval	31±1	31±1	0.646
Atrial characteristic			
$AERP_{100ms}$	28±2	27±2	0.817
Sinus node function			
$SNRT_{100ms}$	191±17	180±8	0.570
$SNRT_{80ms}$	192±16	185±9	0.721
Atrioventricular node function			
$AVERP_{100ms}$	54±7	49±3	0.501
WCL	84±3	83±2	0.763
2:1 CL	60±2	59±2	0.884

Data are means ± SEM from three independent experiments, two-tailed Student's *t* test. 2:1 CL, 2:1 conduction cycle length; AERP, atrial effective refractory period; AVERP, atrioventricular node effective refractory period; BCL, basic cycle length; SNRT, sinus node recovery time; WCL, Wenckebach cycle length.

Table S10. Flow cytometry antibodies.

Antibody	Source	Identifier	Final concentration (µg/ml)
BV605 rat anti-mouse CCR2 (clone SA203G11)	BioLegend	Cat# 150615; RRID AB_2721549	0.80
PerCP/Cy5.5 rat anti-mouse CD9 (clone MZ3)	BioLegend	Cat# 124818; RRID AB_2783077	0.33
APC/Cy7 rat anti-mouse CD11b (clone M1/70)	BioLegend	Cat# 101226; RRID AB_830642	0.33
BV711 rat anti-mouse CD11b (clone M1/70)	BioLegend	Cat# 101242; RRID AB_2563310	0.33
PE/Cy7 rat anti-mouse CD19 (clone 1D3)	ThermoFisher Scientific	Cat# 25-0193-82; RRID AB_657663	0.33
PerCP/Cy5.5 rat anti-mouse CD31 (clone 390)	BioLegend	Cat# 102420; RRID AB_10613644	0.50
BV711 rat anti-mouse CD45 (clone 30-F11)	BD Biosciences	Cat# 563709; RRID AB_2687455	0.33
PE/Cy7 mouse anti-mouse CD64 (clone X54-5/7.1)	BioLegend	Cat# 139313; RRID AB_2563903	0.33
PE rat anti-mouse CD90.2 (clone 53-2.1)	BioLegend	Cat# 140308; RRID AB_10641145	0.17
BV421 rat anti-mouse CD115 (clone AFS98)	BioLegend	Cat# 135513; RRID AB_2562667	0.33
FITC rat anti-mouse CD146 (clone ME-9F1)	BioLegend	Cat# 134706; RRID AB_2143525	0.83
BV570 rat anti-mouse Ly6C (clone HK1.4)	BioLegend	Cat# 128030; RRID AB_2562617	0.33
APC rat anti-mouse Ly6G (clone 1A8)	BioLegend	Cat# 127614; RRID AB_2227348	0.33
PerCP/Cy5.5 rat anti-mouse Ly6G (clone 1A8)	BioLegend	Cat# 127616; RRID AB_1877271	0.33
APC rat anti-mouse MEFSK4 (clone mEF-SK4)	Miltenyi Biotech	Cat# 130-120-802; RRID AB_2784336	1.50
AF700 rat anti-mouse MHCII (M5/114.15.2)	BioLegend	Cat# 107622; RRID AB_493727	0.83
APC rat anti-mouse TREM2 (clone 237920)	R&D Systems	Cat# FAB17291A; RRID AB_884527	1.25

Table S11. Histology antibodies.

	Source	Identifier	Final concentration (µg/ml)
Primary antibodies			
FITC mouse anti-mouse αSMA (clone 1A4)	Sigma-Aldrich	Cat# F3777; RRID AB_476977	4.6
Rabbit anti-mouse collagen I	Abcam	Cat# ab21286; RRID AB_446161	23
Rat anti-mouse CD68 (clone FA-11)	BioLegend	Cat# 137001; RRID AB_2044003	10
Rabbit anti-mouse Ki67 (clone SP6)	ThermoFisher Scientific	Cat# MA5-14520; RRID AB_10979488	1.2
Mouse anti-human CCR2 (clone 7A7)	LifeSpan BioSciences	Cat# LS-C755603; RRID AB_2936515	8.0
Rabbit anti-human CD68	ThermoFisher Scientific	Cat# PA5-83940; RRID AB_2791092	3.2
Rabbit anti-human COL1A1 (clone E8F4L)	Cell Signaling	Cat# 72026S; RRID AB_2904565	0.14
Mouse anti-human SPP1 (clone 7C5H12)	Abcam	Cat# ab166709; RRID AB_2936514	10
Secondary antibodies			
Alexa Fluor 488 goat anti-rabbit IgG	ThermoFisher Scientific	Cat# A-11034; RRID AB_2576217	20
Alexa Fluor 488 goat anti-rat IgG	ThermoFisher Scientific	Cat# A-11006; RRID AB_2534074	20
Biotin goat anti-rabbit IgG	Vector Laboratories	Cat# BA-1000-1.5; RRID AB_2313606	15
Biotin horse anti-mouse IgG	Vector Laboratories	Cat# BA-2000-1.5; RRID AB_2313581	15
DyLight 594 streptavidin	Vector Laboratories	Cat# SA5594-1	1.7

Data S1.
List of significant GOBP gene sets up- or downregulated in seven AFib samples from GSEA of human MP/DC cluster.

Data S2.
List of genes in the three gene modules significantly associated with diseased state in human MP/DC cluster and the C2 gene sets significantly overrepresented in module 1.

Data S3.
List of DEGs in MP/DC, neutrophil, lymphocyte, fibroblast, endothelial and mural cell subsets comparing seven AFib patients with five controls.

Data S4.
List of significant GOBP gene sets up- or downregulated in seven AFib samples from GSEA of human lymphocyte, fibroblast, endothelial and mural cell clusters.

Data S5.
List of marker genes specific to human mono(b) cluster in 10,555 MP/DCs from five controls and seven AFib patients.

Data S6.
List of DEGs in five human macrophage subclusters comparing a subcluster against all other macrophages.

Data S7.
List of C5 GOBP gene sets and their $-\log_{10}$(FDR) values in human and mouse MP/DC clusters.

Data S8.
List of DEGs in LA and LV MP/DC, fibroblast and endothelial cell subsets comparing four HOMER mice with four sham controls.

Data S9.
List of C5 GOBP gene sets and their $-\log_{10}$(FDR) values in human and mouse fibroblast clusters.

References and Notes

1. M. Litviňuková, C. Talavera-López, H. Maatz, D. Reichart, C. L. Worth, E. L. Lindberg, M. Kanda, K. Polanski, M. Heinig, M. Lee, E. R. Nadelmann, K. Roberts, L. Tuck, E. S. Fasouli, D. M. DeLaughter, B. McDonough, H. Wakimoto, J. M. Gorham, S. Samari, K. T. Mahbubani, K. Saeb-Parsy, G. Patone, J. J. Boyle, H. Zhang, H. Zhang, A. Viveiros, G. Y. Oudit, O. A. Bayraktar, J. G. Seidman, C. E. Seidman, M. Noseda, N. Hubner, S. A. Teichmann, Cells of the adult human heart. *Nature* **588**, 466–472 (2020).

2. J. A. Nicolás-Ávila, A. Hidalgo, I. Ballesteros, Specialized functions of resident macrophages in brain and heart. *J. Leukoc. Biol.* **104**, 743–756 (2018).

3. E. Forte, M. B. Furtado, N. Rosenthal, The interstitium in cardiac repair: Role of the immune-stromal cell interplay. *Nat. Rev. Cardiol.* **15**, 601–616 (2018).

4. E. J. Benjamin, P. Muntner, A. Alonso, M. S. Bittencourt, C. W. Callaway, A. P. Carson, A. M. Chamberlain, A. R. Chang, S. Cheng, S. R. Das, F. N. Delling, L. Djousse, M. S. V. Elkind, J. F. Ferguson, M. Fornage, L. C. Jordan, S. S. Khan, B. M. Kissela, K. L. Knutson, T. W. Kwan, D. T. Lackland, T. T. Lewis, J. H. Lichtman, C. T. Longenecker, M. S. Loop, P. L. Lutsey, S. S. Martin, K. Matsushita, A. E. Moran, M. E. Mussolino, M. O'Flaherty, A. Pandey, A. M. Perak, W. D. Rosamond, G. A. Roth, U. K. A. Sampson, G. M. Satou, E. B. Schroeder, S. H. Shah, N. L. Spartano, A. Stokes, D. L. Tirschwell, C. W. Tsao, M. P. Turakhia, L. B. VanWagner, J. T. Wilkins, S. S. Wong, S. S. Virani, American Heart Association Council on Epidemiology and Prevention Statistics Committee and Stroke Statistics Subcommittee, Heart Disease and Stroke Statistics-2019 Update: A Report From the American Heart Association. *Circulation* **139**, e56–e528 (2019).

5. T. Yamashita, A. Sekiguchi, Y. K. Iwasaki, T. Date, K. Sagara, H. Tanabe, H. Suma, H. Sawada, T. Aizawa, Recruitment of immune cells across atrial endocardium in human atrial fibrillation. *Circ. J.* **74**, 262–270 (2010).

6. N. Smorodinova, M. Bláha, V. Melenovský, K. Rozsívalová, J. Přidal, M. Ďurišová, J. Pirk, J. Kautzner, T. Kučera, Analysis of immune cell populations in atrial myocardium of patients with atrial fibrillation or sinus rhythm. *PLOS ONE* **12**, e0172691 (2017).

7. C. Yao, T. Veleva, L. Scott Jr., S. Cao, L. Li, G. Chen, P. Jeyabal, X. Pan, K. M. Alsina, I. Abu-Taha, S. Ghezelbash, C. L. Reynolds, Y. H. Shen, S. A. LeMaire, W. Schmitz, F. U. Müller, A. El-Armouche, N. Tony Eissa, C. Beeton, S. Nattel, X. H. T. Wehrens, D. Dobrev, N. Li, Enhanced Cardiomyocyte NLRP3 Inflammasome Signaling Promotes Atrial Fibrillation. *Circulation* **138**, 2227–2242 (2018).

8. Y. K. Iwasaki, K. Nishida, T. Kato, S. Nattel, Atrial fibrillation pathophysiology: Implications for management. *Circulation* **124**, 2264–2274 (2011).

9. V. Rudolph, R. P. Andrié, T. K. Rudolph, K. Friedrichs, A. Klinke, B. Hirsch-Hoffmann, A. P. Schwoerer, D. Lau, X. Fu, K. Klingel, K. Sydow, M. Didié, A. Seniuk, E.-C. von Leitner, K. Szoecs, J. W. Schrickel, H. Treede, U. Wenzel, T. Lewalter, G. Nickenig, W.-H. Zimmermann, T. Meinertz, R. H. Böger, H. Reichenspurner, B. A. Freeman, T. Eschenhagen, H. Ehmke, S. L. Hazen, S. Willems, S. Baldus, Myeloperoxidase acts as a profibrotic mediator of atrial fibrillation. *Nat. Med.* **16**, 470–474 (2010).

10. M. D. Robinson, D. J. McCarthy, G. K. Smyth, edgeR: A Bioconductor package for differential expression analysis of digital gene expression data. *Bioinformatics* **26**, 139–140 (2010).

11. A. Subramanian, P. Tamayo, V. K. Mootha, S. Mukherjee, B. L. Ebert, M. A. Gillette, A. Paulovich, S. L. Pomeroy, T. R. Golub, E. S. Lander, J. P. Mesirov, Gene set enrichment analysis: A knowledge-based approach for interpreting genome-wide expression profiles. *Proc. Natl. Acad. Sci. U.S.A.* **102**, 15545–15550 (2005).

12. P. Langfelder, S. Horvath, WGCNA: An R package for weighted correlation network analysis. *BMC Bioinformatics* **9**, 559 (2008).

13. N. G. Frangogiannis, Matricellular proteins in cardiac adaptation and disease. *Physiol. Rev.* **92**, 635–688 (2012).

14. I. F. Charo, R. M. Ransohoff, The many roles of chemokines and chemokine receptors in inflammation. *N. Engl. J. Med.* **354**, 610–621 (2006).

15. M. Hulsmans, H. B. Sager, J. D. Roh, M. Valero-Muñoz, N. E. Houstis, Y. Iwamoto, Y. Sun, R. M. Wilson, G. Wojtkiewicz, B. Tricot, M. T. Osborne, J. Hung, C. Vinegoni, K. Naxerova, D. E. Sosnovik, M. R. Zile, A. D. Bradshaw, R. Liao, A. Tawakol, R. Weissleder, A. Rosenzweig, F. K. Swirski, F. Sam, M. Nahrendorf, Cardiac macrophages promote diastolic dysfunction. *J. Exp. Med.* **215**, 423–440 (2018).

16. N. V. Serbina, E. G. Pamer, Monocyte emigration from bone marrow during bacterial infection requires signals mediated by chemokine receptor CCR2. *Nat. Immunol.* **7**, 311–317 (2006).

17. X. Tang, X.-F. Chen, N.-Y. Wang, X.-M. Wang, S.-T. Liang, W. Zheng, Y.-B. Lu, X. Zhao, D.-L. Hao, Z.-Q. Zhang, M.-H. Zou, D.-P. Liu, H.-Z. Chen, SIRT2 acts as a cardioprotective deacetylase in pathological cardiac hypertrophy. *Circulation* **136**, 2051–2067 (2017).

18. X. Liao, Y. Shen, R. Zhang, K. Sugi, N. T. Vasudevan, M. A. Alaiti, D. R. Sweet, L. Zhou, Y. Qing, S. L. Gerson, C. Fu, A. Wynshaw-Boris, R. Hu, M. A. Schwartz, H. Fujioka, B. Richardson, M. J. Cameron, H. Hayashi, J. S. Stamler, M. K. Jain, Distinct roles of resident and nonresident macrophages in nonischemic cardiomyopathy. *Proc. Natl. Acad. Sci. U.S.A.* **115**, E4661–E4669 (2018).

19. Q. Zhang, K. Zhao, Q. Shen, Y. Han, Y. Gu, X. Li, D. Zhao, Y. Liu, C. Wang, X. Zhang, X. Su, J. Liu, W. Ge, R. L. Levine, N. Li, X. Cao, Tet2 is required to resolve inflammation by recruiting Hdac2 to specifically repress IL-6. *Nature* **525**, 389–393 (2015).

20. D. M. Hardbower, M. Asim, P. B. Luis, K. Singh, D. P. Barry, C. Yang, M. A. Steeves, J. L. Cleveland, C. Schneider, M. B. Piazuelo, A. P. Gobert, K. T. Wilson, Ornithine decarboxylase regulates M1 macrophage activation and mucosal inflammation via histone modifications. *Proc. Natl. Acad. Sci. U.S.A.* **114**, E751–E760 (2017).

21. E. K. Koltsova, C. C. Hedrick, K. Ley, Myeloid cells in atherosclerosis: A delicate balance of anti-inflammatory and proinflammatory mechanisms. *Curr. Opin. Lipidol.* **24**, 371–380 (2013).

22. P. Ramachandran, R. Dobie, J. R. Wilson-Kanamori, E. F. Dora, B. E. P. Henderson, N. T. Luu, J. R. Portman, K. P. Matchett, M. Brice, J. A. Marwick, R. S. Taylor, M. Efremova, R. Vento-Tormo, N. O. Carragher, T. J. Kendall, J. A. Fallowfield, E. M. Harrison, D. J. Mole, S. J. Wigmore, P. N. Newsome, C. J. Weston, J. P. Iredale, F. Tacke, J. W. Pollard, C. P. Ponting, J. C. Marioni, S. A. Teichmann, N. C. Henderson, Resolving the fibrotic niche of human liver cirrhosis at single-cell level. *Nature* **575**, 512–518 (2019).

23. R. R. Huxley, F. L. Lopez, A. R. Folsom, S. K. Agarwal, L. R. Loehr, E. Z. Soliman, R. Maclehose, S. Konety, A. Alonso, Absolute and attributable risks of atrial fibrillation in relation to optimal and borderline risk factors: The Atherosclerosis Risk in Communities (ARIC) study. *Circulation* **123**, 1501–1508 (2011).

24. T. S. Tsang, M. E. Barnes, K. R. Bailey, C. L. Leibson, S. C. Montgomery, Y. Takemoto, P. M. Diamond, M. A. Marra, B. J. Gersh, D. O. Wiebers, G. W. Petty, J. B. Seward, Left atrial volume: Important risk marker of incident atrial fibrillation in 1655 older men and women. *Mayo Clin. Proc.* **76**, 467–475 (2001).

25. A. Xintarakou, S. Tzeis, S. Psarras, D. Asvestas, P. Vardas, Atrial fibrosis as a dominant factor for the development of atrial fibrillation: Facts and gaps. *Europace* **22**, 342–351 (2020).

26. J. D. Schilling, H. M. Machkovech, A. H. Kim, R. Schwendener, J. E. Schaffer, Macrophages modulate cardiac function in lipotoxic cardiomyopathy. *Am. J. Physiol. Heart Circ. Physiol.* **303**, H1366–H1373 (2012).

27. L. Wang, Y.-L. Zhang, Q.-Y. Lin, Y. Liu, X.-M. Guan, X.-L. Ma, H.-J. Cao, Y. Liu, J. Bai, Y.-L. Xia, J. Du, H.-H. Li, CXCL1-CXCR2 axis mediates angiotensin II-induced cardiac hypertrophy and remodelling through regulation of monocyte infiltration. *Eur. Heart J.* **39**, 1818–1831 (2018).

28. S. Epelman, K. J. Lavine, A. E. Beaudin, D. K. Sojka, J. A. Carrero, B. Calderon, T. Brija, E. L. Gautier, S. Ivanov, A. T. Satpathy, J. D. Schilling, R. Schwendener, I. Sergin, B. Razani, E. C. Forsberg, W. M. Yokoyama, E. R. Unanue, M. Colonna, G. J. Randolph, D. L. Mann, Embryonic and adult-derived resident cardiac macrophages are maintained through distinct mechanisms at steady state and during inflammation. *Immunity* **40**, 91–104 (2014).

29. G. Bajpai, C. Schneider, N. Wong, A. Bredemeyer, M. Hulsmans, M. Nahrendorf, S. Epelman, D. Kreisel, Y. Liu, A. Itoh, T. S. Shankar, C. H. Selzman, S. G. Drakos, K. J. Lavine, The human heart contains distinct macrophage subsets with divergent origins and functions. *Nat. Med.* **24**, 1234–1245 (2018).

30. L. Ziegler-Heitbrock, P. Ancuta, S. Crowe, M. Dalod, V. Grau, D. N. Hart, P. J. M. Leenen, Y.-J. Liu, G. MacPherson, G. J. Randolph, J. Scherberich, J. Schmitz, K. Shortman, S. Sozzani, H. Strobl, M. Zembala, J. M. Austyn, M. B. Lutz, Nomenclature of monocytes and dendritic cells in blood. *Blood* **116**, e74–e80 (2010).

31. R. Gopinathannair, L. Y. Chen, M. K. Chung, W. K. Cornwell, K. L. Furie, D. R. Lakkireddy, N. F. Marrouche, A. Natale, B. Olshansky, J. A. Joglar, American Heart Association Electrocardiography and Arrhythmias Committee and Heart Failure and Transplantation Committee of the Council on Clinical Cardiology, Council on Arteriosclerosis, Thrombosis and Vascular Biology, Council on Hypertension, Council

on Lifestyle and Cardiometabolic Health, and the Stroke Council, Managing atrial fibrillation in patients with heart failure and reduced ejection fraction: A scientific statement from the American Heart Association. *Circ. Arrhythm. Electrophysiol.* **14**, HAE0000000000000078 (2021).

32. C. Blériot, S. Chakarov, F. Ginhoux, Determinants of resident tissue macrophage identity and function. *Immunity* **52**, 957–970 (2020).

33. F. F. Hoyer, K. Naxerova, M. J. Schloss, M. Hulsmans, A. V. Nair, P. Dutta, D. M. Calcagno, F. Herisson, A. Anzai, Y. Sun, G. Wojtkiewicz, D. Rohde, V. Frodermann, K. Vandoorne, G. Courties, Y. Iwamoto, C. S. Garris, D. L. Williams, S. Breton, D. Brown, M. Whalen, P. Libby, M. J. Pittet, K. R. King, R. Weissleder, F. K. Swirski, M. Nahrendorf, Tissue-specific macrophage responses to remote injury impact the outcome of subsequent local immune challenge. *Immunity* **51**, 899–914.e7 (2019).

34. S. Epelman, K. J. Lavine, G. J. Randolph, Origin and functions of tissue macrophages. *Immunity* **41**, 21–35 (2014).

35. C. D. Paavola, S. Hemmerich, D. Grunberger, I. Polsky, A. Bloom, R. Freedman, M. Mulkins, S. Bhakta, D. McCarley, L. Wiesent, B. Wong, K. Jarnagin, T. M. Handel, Monomeric monocyte chemoattractant protein-1 (MCP-1) binds and activates the MCP-1 receptor CCR2B. *J. Biol. Chem.* **273**, 33157–33165 (1998).

36. M. Efremova, M. Vento-Tormo, S. A. Teichmann, R. Vento-Tormo, CellPhoneDB: Inferring cell-cell communication from combined expression of multi-subunit ligand-receptor complexes. *Nat. Protoc.* **15**, 1484–1506 (2020).

37. M. Harada, S. Nattel, Implications of inflammation and fibrosis in atrial fibrillation pathophysiology. *Card. Electrophysiol. Clin.* **13**, 25–35 (2021).

38. K. Graf, M. Neuss, P. Stawowy, W. A. Hsueh, E. Fleck, R. E. Law, Angiotensin II and alpha(v)beta(3) integrin expression in rat neonatal cardiac fibroblasts. *Hypertension* **35**, 978–984 (2000).

39. V. Sarrazy, A. Koehler, M. L. Chow, E. Zimina, C. X. Li, H. Kato, C. A. Caldarone, B. Hinz, Integrins αvβ5 and αvβ3 promote latent TGF-β1 activation by human cardiac fibroblast contraction. *Cardiovasc. Res.* **102**, 407–417 (2014).

40. J. Molvin, A. Jujic, O. Melander, M. Pareek, L. Råstam, U. Lindblad, B. Daka, M. Leosdottir, P. Nilsson, M. Olsen, M. Magnusson, Exploration of pathophysiological pathways for incident atrial fibrillation using a multiplex proteomic chip. *Open Heart* **7**, e001190 (2020).

41. L. Liaw, D. E. Birk, C. B. Ballas, J. S. Whitsitt, J. M. Davidson, B. L. Hogan, Altered wound healing in mice lacking a functional osteopontin gene (spp1). *J. Clin. Invest.* **101**, 1468–1478 (1998).

42. S. R. Künzel, M. Hoffmann, S. Weber, K. Künzel, S. Kämmerer, M. Günscht, E. Klapproth, J. S. E. Rausch, M. S. Sadek, T. Kolanowski, S. Meyer-Roxlau, C. Piorkowski, S. M. Tugtekin, S. Rose-John, X. Yin, M. Mayr, J. D. Kuhlmann, P. Wimberger, K. Grützmann, N. Herzog, J.-H. Küpper, M. O'Reilly, S. N. Kabir, L. C. Sommerfeld, K. Guan, B. Wielockx, L. Fabritz, S. Nattel, U. Ravens, D. Dobrev, M. Wagner, A. El-

Armouche, Diminished PLK2 induces cardiac fibrosis and promotes atrial fibrillation. *Circ. Res.* **129**, 804–820 (2021).

43. A. R. Collins, J. Schnee, W. Wang, S. Kim, M. C. Fishbein, D. Bruemmer, R. E. Law, S. Nicholas, R. S. Ross, W. A. Hsueh, Osteopontin modulates angiotensin II-induced fibrosis in the intact murine heart. *J. Am. Coll. Cardiol.* **43**, 1698–1705 (2004).

44. Y. Matsui, N. Jia, H. Okamoto, S. Kon, H. Onozuka, M. Akino, L. Liu, J. Morimoto, S. R. Rittling, D. Denhardt, A. Kitabatake, T. Uede, Role of osteopontin in cardiac fibrosis and remodeling in angiotensin II-induced cardiac hypertrophy. *Hypertension* **43**, 1195–1201 (2004).

45. B. López, A. González, D. Lindner, D. Westermann, S. Ravassa, J. Beaumont, I. Gallego, A. Zudaire, C. Brugnolaro, R. Querejeta, M. Larman, C. Tschöpe, J. Díez, Osteopontin-mediated myocardial fibrosis in heart failure: A role for lysyl oxidase? *Cardiovasc. Res.* **99**, 111–120 (2013).

46. J. A. Nicolás-Ávila, A. V. Lechuga-Vieco, L. Esteban-Martínez, M. Sánchez-Díaz, E. Díaz-García, D. J. Santiago, A. Rubio-Ponce, J. L. Li, A. Balachander, J. A. Quintana, R. Martínez-de-Mena, B. Castejón-Vega, A. Pun-García, P. G. Través, E. Bonzón-Kulichenko, F. García-Marqués, L. Cussó, N. A-González, A. González-Guerra, M. Roche-Molina, S. Martin-Salamanca, G. Crainiciuc, G. Guzmán, J. Larrazabal, E. Herrero-Galán, J. Alegre-Cebollada, G. Lemke, C. V. Rothlin, L. J. Jimenez-Borreguero, G. Reyes, A. Castrillo, M. Desco, P. Muñoz-Cánoves, B. Ibáñez, M. Torres, L. G. Ng, S. G. Priori, H. Bueno, J. Vázquez, M. D. Cordero, J. A. Bernal, J. A. Enríquez, A. Hidalgo, A network of macrophages supports mitochondrial homeostasis in the heart. *Cell* **183**, 94–109.e23 (2020).

47. M. Hulsmans, S. Clauss, L. Xiao, A. D. Aguirre, K. R. King, A. Hanley, W. J. Hucker, E. M. Wülfers, G. Seemann, G. Courties, Y. Iwamoto, Y. Sun, A. J. Savol, H. B. Sager, K. J. Lavine, G. A. Fishbein, D. E. Capen, N. Da Silva, L. Miquerol, H. Wakimoto, C. E. Seidman, J. G. Seidman, R. I. Sadreyev, K. Naxerova, R. N. Mitchell, D. Brown, P. Libby, R. Weissleder, F. K. Swirski, P. Kohl, C. Vinegoni, D. J. Milan, P. T. Ellinor, M. Nahrendorf, Macrophages facilitate electrical conduction in the heart. *Cell* **169**, 510–522.e20 (2017).

48. M. Ashburner, C. A. Ball, J. A. Blake, D. Botstein, H. Butler, J. M. Cherry, A. P. Davis, K. Dolinski, S. S. Dwight, J. T. Eppig, M. A. Harris, D. P. Hill, L. Issel-Tarver, A. Kasarskis, S. Lewis, J. C. Matese, J. E. Richardson, M. Ringwald, G. M. Rubin, G. Sherlock, The Gene Ontology Consortium, Gene Ontology: Tool for the unification of biology. *Nat. Genet.* **25**, 25–29 (2000).

49. S. Carbon, E. Douglass, B. M. Good, D. R. Unni, N. L. Harris, C. J. Mungall, S. Basu, R. L. Chisholm, R. J. Dodson, E. Hartline, P. Fey, P. D. Thomas, L.-P. Albou, D. Ebert, M. J. Kesling, H. Mi, A. Muruganujan, X. Huang, T. Mushayahama, S. A. LaBonte, D. A. Siegele, G. Antonazzo, H. Attrill, N. H. Brown, P. Garapati, S. J. Marygold, V. Trovisco, G. dos Santos, K. Falls, C. Tabone, P. Zhou, J. L. Goodman, V. B. Strelets, J. Thurmond, P. Garmiri, R. Ishtiaq, M. Rodríguez-López, M. L. Acencio, M. Kuiper, A. Lægreid, C. Logie, R. C. Lovering, B. Kramarz, S. C. C. Saverimuttu, S. M. Pinheiro, H. Gunn, R. Su, K. E. Thurlow, M. Chibucos, M. Giglio, S. Nadendla, J. Munro, R. Jackson, M. J.

Duesbury, N. Del-Toro, B. H. M. Meldal, K. Paneerselvam, L. Perfetto, P. Porras, S. Orchard, A. Shrivastava, H.-Y. Chang, R. D. Finn, A. L. Mitchell, N. D. Rawlings, L. Richardson, A. Sangrador-Vegas, J. A. Blake, K. R. Christie, M. E. Dolan, H. J. Drabkin, D. P. Hill, L. Ni, D. M. Sitnikov, M. A. Harris, S. G. Oliver, K. Rutherford, V. Wood, J. Hayles, J. Bähler, E. R. Bolton, J. L. De Pons, M. R. Dwinell, G. T. Hayman, M. L. Kaldunski, A. E. Kwitek, S. J. F. Laulederkind, C. Plasterer, M. A. Tutaj, M. Vedi, S.-J. Wang, P. D'Eustachio, L. Matthews, J. P. Balhoff, S. A. Aleksander, M. J. Alexander, J. M. Cherry, S. R. Engel, F. Gondwe, K. Karra, S. R. Miyasato, R. S. Nash, M. Simison, M. S. Skrzypek, S. Weng, E. D. Wong, M. Feuermann, P. Gaudet, A. Morgat, E. Bakker, T. Z. Berardini, L. Reiser, S. Subramaniam, E. Huala, C. N. Arighi, A. Auchincloss, K. Axelsen, G. Argoud-Puy, A. Bateman, M.-C. Blatter, E. Boutet, E. Bowler, L. Breuza, A. Bridge, R. Britto, H. Bye-A-Jee, C. C. Casas, E. Coudert, P. Denny, A. Estreicher, M. L. Famiglietti, G. Georghiou, A. Gos, N. Gruaz-Gumowski, E. Hatton-Ellis, C. Hulo, A. Ignatchenko, F. Jungo, K. Laiho, P. Le Mercier, D. Lieberherr, A. Lock, Y. Lussi, A. MacDougall, M. Magrane, M. J. Martin, P. Masson, D. A. Natale, N. Hyka-Nouspikel, S. Orchard, I. Pedruzzi, L. Pourcel, S. Poux, S. Pundir, C. Rivoire, E. Speretta, S. Sundaram, N. Tyagi, K. Warner, R. Zaru, C. H. Wu, A. D. Diehl, J. N. Chan, C. Grove, R. Y. N. Lee, H.-M. Muller, D. Raciti, K. Van Auken, P. W. Sternberg, M. Berriman, M. Paulini, K. Howe, S. Gao, A. Wright, L. Stein, D. G. Howe, S. Toro, M. Westerfield, P. Jaiswal, L. Cooper, J. Elser; Gene Ontology Consortium, The Gene Ontology resource: Enriching a GOld mine. *Nucleic Acids Res.* **49** (D1), D325–D334 (2021).

50. A. Liberzon, C. Birger, H. Thorvaldsdóttir, M. Ghandi, J. P. Mesirov, P. Tamayo, The Molecular Signatures Database (MSigDB) hallmark gene set collection. *Cell Syst.* **1**, 417–425 (2015).

51. S. Kou, L. Caballero, R. Dulgheru, D. Voilliot, C. De Sousa, G. Kacharava, G. D. Athanassopoulos, D. Barone, M. Baroni, N. Cardim, J. J. Gomez De Diego, A. Hagendorff, C. Henri, K. Hristova, T. Lopez, J. Magne, G. De La Morena, B. A. Popescu, M. Penicka, T. Ozyigit, J. D. Rodrigo Carbonero, A. Salustri, N. Van De Veire, R. S. Von Bardeleben, D. Vinereanu, J.-U. Voigt, J. L. Zamorano, E. Donal, R. M. Lang, L. P. Badano, P. Lancellotti, Echocardiographic reference ranges for normal cardiac chamber size: Results from the NORRE study. *Eur. Heart J. Cardiovasc. Imaging* **15**, 680–690 (2014).

52. Echocardiographic Normal Ranges Meta-Analysis of the Left Heart Collaboration, Ethnic-specific normative reference values for echocardiographic LA and LV size, LV mass, and systolic function: The EchoNoRMAL Study. *JACC Cardiovasc. Imaging* **8**, 656–665 (2015).

53. A. R. Pinto, A. Ilinykh, M. J. Ivey, J. T. Kuwabara, M. L. D'Antoni, R. Debuque, A. Chandran, L. Wang, K. Arora, N. A. Rosenthal, M. D. Tallquist, Revisiting cardiac cellular composition. *Circ. Res.* **118**, 400–409 (2016).

54. D. A. Skelly, G. T. Squiers, M. A. McLellan, M. T. Bolisetty, P. Robson, N. A. Rosenthal, A. R. Pinto, Single-cell transcriptional profiling reveals cellular diversity and intercommunication in the mouse heart. *Cell Rep.* **22**, 600–610 (2018).

55. T. Stuart, A. Butler, P. Hoffman, C. Hafemeister, E. Papalexi, W. M. Mauck III, Y. Hao, M. Stoeckius, P. Smibert, R. Satija, Comprehensive integration of single-cell data. *Cell* **177**, 1888–1902.e21 (2019).

56. A. Butler, P. Hoffman, P. Smibert, E. Papalexi, R. Satija, Integrating single-cell transcriptomic data across different conditions, technologies, and species. *Nat. Biotechnol.* **36**, 411–420 (2018).

57. C. Hafemeister, R. Satija, Normalization and variance stabilization of single-cell RNA-seq data using regularized negative binomial regression. *Genome Biol.* **20**, 296 (2019).

58. A. T. L. Lun, J. C. Marioni, Overcoming confounding plate effects in differential expression analyses of single-cell RNA-seq data. *Biostatistics* **18**, 451–464 (2017).

59. Y. Chen, A. T. Lun, G. K. Smyth, From reads to genes to pathways: Differential expression analysis of RNA-Seq experiments using Rsubread and the edgeR quasi-likelihood pipeline. *F1000Res.* **5**, 1438 (2016).

60. D. J. McCarthy, Y. Chen, G. K. Smyth, Differential expression analysis of multifactor RNA-Seq experiments with respect to biological variation. *Nucleic Acids Res.* **40**, 4288–4297 (2012).

61. V. K. Mootha, C. M. Lindgren, K.-F. Eriksson, A. Subramanian, S. Sihag, J. Lehar, P. Puigserver, E. Carlsson, M. Ridderstråle, E. Laurila, N. Houstis, M. J. Daly, N. Patterson, J. P. Mesirov, T. R. Golub, P. Tamayo, B. Spiegelman, E. S. Lander, J. N. Hirschhorn, D. Altshuler, L. C. Groop, PGC-1α-responsive genes involved in oxidative phosphorylation are coordinately downregulated in human diabetes. *Nat. Genet.* **34**, 267–273 (2003).

62. A. Liberzon, A. Subramanian, R. Pinchback, H. Thorvaldsdóttir, P. Tamayo, J. P. Mesirov, Molecular signatures database (MSigDB) 3.0. *Bioinformatics* **27**, 1739–1740 (2011).

63. B. Zhang, S. Horvath, A general framework for weighted gene co-expression network analysis. *Stat. Appl. Genet. Mol. Biol.* **4**, e17 (2005).

64. E. I. Boyle, S. Weng, J. Gollub, H. Jin, D. Botstein, J. M. Cherry, G. Sherlock, GO:TermFinder—Open source software for accessing Gene Ontology information and finding significantly enriched Gene Ontology terms associated with a list of genes. *Bioinformatics* **20**, 3710–3715 (2004).

65. T. Wu, E. Hu, S. Xu, M. Chen, P. Guo, Z. Dai, T. Feng, L. Zhou, W. Tang, L. Zhan, X. Fu, S. Liu, X. Bo, G. Yu, clusterProfiler 4.0: A universal enrichment tool for interpreting omics data. *Innovation* **2**, 100141 (2021).

66. R. Vento-Tormo, M. Efremova, R. A. Botting, M. Y. Turco, M. Vento-Tormo, K. B. Meyer, J.-E. Park, E. Stephenson, K. Polański, A. Goncalves, L. Gardner, S. Holmqvist, J. Henriksson, A. Zou, A. M. Sharkey, B. Millar, B. Innes, L. Wood, A. Wilbrey-Clark, R. P. Payne, M. A. Ivarsson, S. Lisgo, A. Filby, D. H. Rowitch, J. N. Bulmer, G. J. Wright, M. J. T. Stubbington, M. Haniffa, A. Moffett, S. A. Teichmann, Single-cell reconstruction of the early maternal-fetal interface in humans. *Nature* **563**, 347–353 (2018).

67. C. S. McAlpine, J. Park, A. Griciuc, E. Kim, S. H. Choi, Y. Iwamoto, M. G. Kiss, K. A. Christie, C. Vinegoni, W. C. Poller, J. E. Mindur, C. T. Chan, S. He, H. Janssen, L. P.

Wong, J. Downey, S. Singh, A. Anzai, F. Kahles, M. Jorfi, P. F. Feruglio, R. I. Sadreyev, R. Weissleder, B. P. Kleinstiver, M. Nahrendorf, R. E. Tanzi, F. K. Swirski, Astrocytic interleukin-3 programs microglia and limits Alzheimer's disease. *Nature* **595**, 701–706 (2021).